




Janus piezoelectric adhesives regulate macrophage TRPV1/Ca²⁺/cAMP axis to stimulate tendon-to-bone healing by multi-omics analysis

Moran Huang^{a,1}, Wan Li^{b,1}, Yaying Sun^{a,1}, Jize Dong^a, Chaojing Li^b, Henjie Jia^a, Yongjie Jiao^b, Lu Wang^b, Shanxing Zhang^{a,*}, Fujun Wang^{b,c,**}, Jiwu Chen^{a,***} 

^a Department of Sports Medicine, Shanghai General Hospital, Shanghai Jiao Tong University School of Medicine, Shanghai, 200080, China

^b Key Laboratory of Textile Science & Technology, Ministry of Education, Donghua University, Shanghai, 201620, China

^c Shanghai Frontiers Science Center of Advanced Textiles, College of Textiles, Donghua University, Shanghai 201620, China

ARTICLE INFO

Keywords:

Piezoelectric biomaterials
Tendon-to-bone healing
Immunomodulation
Asymmetric adhesive hydrogel
TRP channels

ABSTRACT

Piezoelectric stimulation has garnered substantial interest as a promising strategy for tissue regeneration. However, studies investigating its impact on tendon-to-bone healing characterized by fibrocartilage remain scarce. Moreover, there are considerable technical challenges in achieving minimally invasive application of piezoelectric stimulation on the irregular tendon-to-bone interface. Herein, we developed Janus asymmetric piezoelectric adhesives by assembling adhesive hydrogel (GAN) and non-adhesive hydrogel (GM) on each side of piezoelectric poly (L-lactic acid) nanofiber. Piezoelectric adhesives exhibited superior anti-inflammatory effects both *in vitro* and *ex vivo*. Notably, the transient receptor potential (TRP) ion channels, a class of versatile signaling molecules, are closely associated with the regulation of inflammation. This study demonstrated that piezoelectric stimulation promoted Ca²⁺ influx through the activation of transient receptor potential vanilloid 1 (TRPV1), further enhancing cAMP signaling pathway in macrophages by RNA sequencing. Additionally, *in vivo* proteomic analysis revealed Arachidonic acid metabolism and TNF- α signaling pathway downregulation and VEGF signaling pathway upregulation in a rat rotator cuff repair model. Piezoelectric adhesives ultimately achieved inflammation alleviation, angiogenesis enhancement, and fibrocartilage regeneration promotion, improving the biomechanical strength of the enthesis. This study elucidated the mechanism by which piezoelectric stimulation regulated tendon-to-bone healing through multi-omics analysis. The piezoelectric adhesives hold promise as a convenient and effective strategy for enhancing tendon-to-bone healing in clinical practice.

1. Introduction

Rotator cuff tears are very common musculoskeletal disorders leading to shoulder pain and functional impairment. The incidence exceeds 20 % and escalates with age in the population [1]. Arthroscopic rotator cuff repair (RCR) is currently considered the preferred intervention for patients who fail to achieve relief from conservative treatment [2]. However, the retear rate following surgery remains alarmingly high, ranging from 20 % to 94 % [3]. This is often attributed to the formation

of scar tissue at the tendon-to-bone interface, which replaces the natural fibrocartilage structure and results in a reduction of mechanical performance by approximately 50 % [4]. Such outcomes are closely associated with factors including the postoperative immune microenvironment and inadequate blood supply at the tendon-to-bone interface [5]. Therefore, the high-quality reconstruction of the fibrocartilage layer at the tendon-to-bone interface is crucial for promoting tendon healing while simultaneously reducing the retear rate following rotator cuff surgery.

Peer review under the responsibility of editorial board of Bioactive Materials.

* Corresponding author.

** Corresponding author.

*** Corresponding author.

E-mail addresses: huangmoran44@126.com (M. Huang), liwan0504@163.com (W. Li), yaying.sun@shgh.cn (Y. Sun), djz9975@163.com (J. Dong), lcj@dhu.edu.cn (C. Li), wilbert@sjtu.edu.cn (H. Jia), 15021072910@163.com (Y. Jiao), wanglu@dhu.edu.cn (L. Wang), zhangshanxing1984@163.com (S. Zhang), wangfujun@dhu.edu.cn (F. Wang), jeevechen@gmail.com (J. Chen).

¹ These authors contributed equally.

<https://doi.org/10.1016/j.bioactmat.2025.03.029>

Received 7 February 2025; Received in revised form 14 March 2025; Accepted 31 March 2025

2452-199X/© 2025 The Authors. Publishing services by Elsevier B.V. on behalf of KeAi Communications Co. Ltd. This is an open access article under the CC BY-NC-ND license (<http://creativecommons.org/licenses/by-nc-nd/4.0/>).

In recent years, tissue engineering technology has increasingly been recognized as a promising strategy for promoting tissue repair such as the rotator cuff. While many studies involving stem cells and bioactive substances therapies were reported to face drawbacks related to biosafety, immunogenicity, and high costs [6]. In contrast, controllable physical stimulation represented by electrical stimulation and magnetic stimulation greatly reduces these risks and might be more conducive to clinical translation [7]. The electrical microenvironment is an integral part of normal physiological activities in human body, electrical stimulation might replenish the disrupted electrical microenvironment at the damaged tissue site, thereby achieving benefits [8]. Current reports indicated that electrical stimulation could directly promote tissue regeneration, particularly in bone and cartilage tissues [9].

Interestingly, electrical stimulation was believed to indirectly enhance tissue repair by modulating inflammatory states [10]. The immune microenvironment, exemplified by macrophages, plays a crucial role in the process of rotator cuff repair. In the early stages, the polarization of M0 macrophages towards the M2 phenotype and the inhibition of excessive secretion of inflammatory factors contribute to angiogenesis and the fibrocartilage regeneration [11]. However, the impact of electrical stimulation on the healing of the tendon-to-bone interface characterized by fibrocartilage remains to be fully investigated. Additionally, the application of external devices to deliver electrical stimulation might weaken due to tissue absorption, and there also exist risks of infection with implanted electrical stimulation devices and the complications caused by the surgical removal of toxic batteries [12]. Piezoelectric materials, which generate electrical energy under mechanical stress (load or ultrasound (US)), present ideal candidate materials for addressing these challenges, demonstrating potential applications across various fields of tissue regeneration [13]. Nevertheless, there are limitations regarding the selection of piezoelectric materials, such as the hazardous substances (e.g., lead zirconate titanate), non-degradable properties (e.g., PVDF), and materials that require further verification of long-term biosafety (BaTiO₃ and potassium sodium niobate) [14]. Poly(L-lactic acid) (PLLA), representative of biodegradable piezoelectric materials, exhibits excellent biosafety and has been widely used in the preparation of FDA-approved bio-scaffolds [13a]. Das et al. reported that PLLA-based piezoelectric scaffolds promoted skin regeneration while safely degrading into non-toxic byproducts [15]. Additionally, Vinikoor et al. recently reported that piezoelectric PLLA with ultrasound-induced stimulation could promote chondrogenesis in rabbits and treat osteoarthritis [13b]. Currently, to the best of our knowledge, ultrasound-induced piezoelectric PLLA stimulation has not been attempted in repairing rotator cuff tears.

Recently, non-invasive methods (e.g., adhesives) for stabilizing scaffolds have attracted considerable interest [16]. Compared to traditionally suturing the scaffold over the rotator cuff tears site, this approach can reduce arthroscopic surgery duration and complexity [17]. In addition, attempts have been made to inject hydrogel-based scaffolds in situ into the tear site; however, joint movement and irregular interfaces make it challenging for hydrogels to stay stably at the injury site [18]. The application of adhesives offers a novel perspective to address these challenges. This non-invasive method allows for the simple adhesion of the scaffold/film to the rotator cuff tear, thus achieving stable fixation. Notably, the adhesive should not only exhibit strong adhesion to the tear site, but also maintain non-adhesive with surrounding tissues (e.g., the deltoid muscle) to ensure normal sliding between muscles. To address this problem, an intriguing concept might be provided by preparing asymmetric Janus adhesive films with adhesive property on one side and non-adhesive property on the other [19]. Among the various design strategies based on chemical bonding, covalent bonds, represented by N-hydroxy succinimide (NHS)-activated ester bonds, were reported to exhibit more stable and stronger adhesive properties compared to non-covalent bonds [16]. Recent studies were demonstrated that the adhesives with N-hydroxy succinimide (NHS) activated ester bonds exhibited excellent biocompatibility and adhesive

capacity [20]. To construct the Janus adhesive, we utilized gelatin and acrylic acid (AA) in combination with N-hydroxy succinimide (NHS) to form the interpenetrating polymer network (IPN) as the adhesive surface. In contrast, the non-adhesive surface was constituted by gelatin and acrylamide (AM).

In this study, we developed a novel "sandwich-structured" Janus asymmetric piezoelectric adhesives, termed Gelatin-Polyacrylic acid-NHS/PLLA/Gelatin-Polyacrylamide (GAN/PLLA/GM) Janus adhesive films (N/P/M). Specifically, PLLA membranes were constructed using electrospinning, GAN and GM were crosslinked with ultraviolet light on each side, respectively. N/P/M exhibited asymmetric adhesive properties and can generate appropriate electrical stimulation under ultrasound induction (Scheme 1A). We investigated its effects on macrophage polarization and the inflammation modulation of human-injured rotator cuff samples, and further explored its role in vascular regulation. Subsequently, we assessed the therapeutic effect of N/P/M on tendon-to-bone healing in a rat rotator cuff repair model. Additionally, this study employed multi-omics analysis, including *in vitro* RNA sequencing and *in vivo* proteomics, to elucidate the molecular mechanisms by which N/P/M regulates inflammation *in vitro* and influences early-stage tendon-to-bone healing *in vivo* (Scheme 1B-C).

2. Experimental section/methods

2.1. Fabrication of oriented PLLA electrospun nanofiber membranes

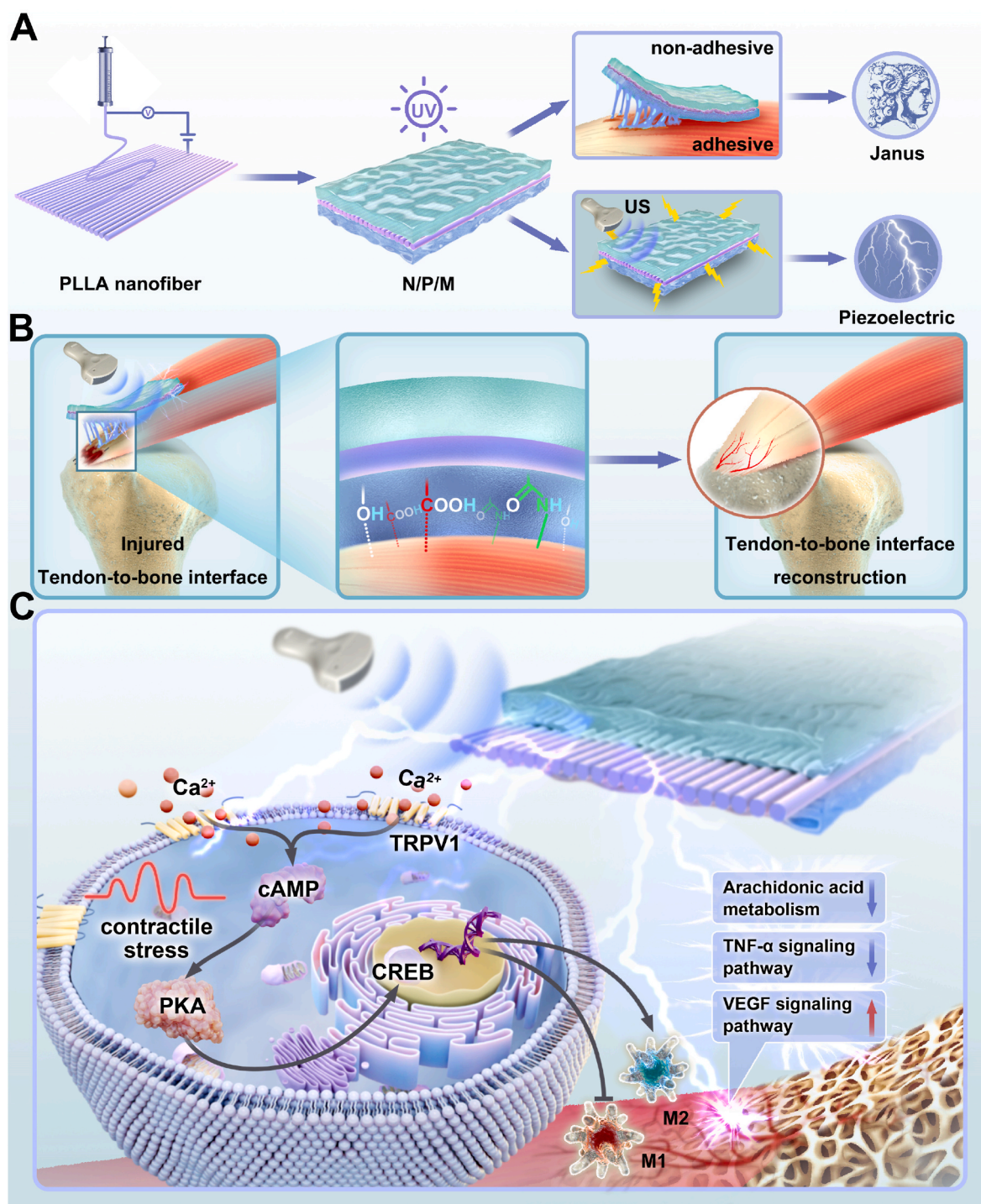
Firstly, piezoelectric PLLA nanofiber mats were fabricated using the electrospinning technique. Specifically, 1 g of PLLA (Corbion Purac, Amsterdam, Netherlands) was dissolved in 20 mL of chloroform (Sigma-Aldrich) overnight to ensure complete dissolution. The resultant polymer solution was then electrospun using a G22 needle at a flow rate of 2 mL/h under an electric field strength of 14 kV. To achieve well-aligned nanofiber mats, the fibers were collected on a rotating drum collector operating at 4000 rpm, with ambient humidity maintained between 25 and 45 %. Following the electrospinning process, the PLLA nanofiber mats were subjected to thermal annealing at 105 °C for an extended period, followed by slow cooling to room temperature. The annealing process was repeated at 160 °C to further optimize the material properties.

2.2. Preparation of N/P/M Janus adhesive films

To prepare the GAN pre-solution, 5 wt% gelatin, 2 wt% AAc-NHS ester, 30 wt% acrylic acid, 0.1 wt% GelMA, and 0.2 wt% α -ketoglutaric acid were dissolved in deionized water at 45 °C under continuous stirring until complete dissolution was achieved. For the preparation of the GM pre-solution, 5 wt% gelatin, 10 wt% acrylamide, 0.1 wt% GelMA, and 0.2 wt% Irgacure 2959 were similarly dissolved in deionized water at 45 °C under continuous stirring until fully dissolved. Both pre-solutions were then cast onto PTFE molds, covered with glass slides, and exposed to UV light at a wavelength of 365 nm for 45 min, resulting in the formation of the respective hydrogels: GAN and GM. For the fabrication of the N/P/M Janus adhesive films, an oriented PLLA nanofiber membrane was placed in a PTFE mold. The GAN pre-solution was added to the upper surface of the PLLA fiber membrane and covered with a glass slide. This assembly was exposed to UV light at 365 nm for 45 min. Subsequently, the GM pre-solution was added to the opposite side of the PLLA nanofiber membrane, again covered with a glass slide, and exposed to UV light at 365 nm for an additional 45 min, thereby obtaining the final N/P/M Janus hydrogel. Dry thickness: 0.3 ± 0.05 mm (measured via micrometer). Hydrated thickness: 1.1 ± 0.10 mm (after 24 h in PBS).

2.3. Morphology and chemical structure analysis

The morphology of the samples was observed using a field emission



Scheme 1. Design and biomedical applications of Janus asymmetric piezoelectric adhesives. A) Preparation and properties of N/P/M Janus adhesive films. B) Usage and adhesion mechanism of N/P/M Janus adhesive films. Dashed lines represent hydrogen bonds, while solid lines represent amide bonds. C) Multi-omics analysis revealing the mechanisms in the application of N/P/M.

scanning electron microscope (FESEM, Hitachi, Japan). The chemical structures of the samples were determined using an FTIR microscopic imaging spectrometer (Nicolet 6700, Thermo Fisher Scientific, USA).

2.4. Piezoelectric performance testing

The dried film samples were cut into 10 × 10 mm squares. Copper tape was used as electrodes and adhered to both sides of the samples to ensure good electrical contact. The electrodes were encapsulated using

polyimide tape (DuPont) to prepare the piezoelectric device. The piezoelectric signal was generated using a handheld ultrasonic device operating at a frequency of 1 MHz (Sonopuls 190), and the piezoelectric performance was measured with an oscilloscope (MSO22, Tektronix). Thermal properties and crystallinity were analyzed using differential scanning calorimetry (CLARUS SQ8-STA8000, PerkinElmer, Netherlands).

2.5. Mechanical property testing and adhesion strength measurement

The stress-strain curves of the samples were obtained using a tensile testing machine (Wenzhou Darong Textile Instrument Co., Ltd., China). All samples were cut into a dumbbell shape and stretched at a rate of 50 mm/min. To characterize mechanical anisotropy, the mechanical properties parallel and perpendicular to the fiber orientation were measured separately. To test the adhesive strength, according to the ASTM F2255 standard lap shear test, the samples and porcine muscle tissue were cut into rectangular shapes with a width of 25 mm, and the adhesive area was set to 25 mm × 10 mm. Cyanoacrylate adhesive was used to attach the tissue and samples to a polydimethylsiloxane (PDMS) plate as a rigid backing. The sample and tissue were brought into contact and pressed for 10 s. Afterwards, tensile testing was performed on a tensile testing machine at a constant speed of 10 mm/min. The detailed testing method and shear strength formula were shown in Fig. 1G.

2.6. Cell culture and viability assay

Tohoku Hospital Pediatrics-1 (THP-1) were obtained from *Procell Life Science & Technology Co., Ltd.* (Shanghai, China) and maintained in RPMI 1640 (Servicebio, China). Human umbilical vein endothelial cells (HUVECs) were acquired from the Chinese Academy of Science (Shanghai, China) and cultured in endothelial cell medium (ECM; Sciencell, USA). Firstly, THP-1 seeded on adhesive films was induced to M0 macrophage with 200 nM 12-O-tetradecanoylphorbol-13-acetate (PMA; Sigma, USA) for 48 h. The viability of M0 macrophages and HUVECs seeded on adhesive films was assessed with a Cell Counting Kit-8 (CCK-8) assay and a live/dead staining kit (Beyotime, China) under different ultrasound power densities (0.5 W/cm² and 1 W/cm²; 1 MHz; 5 min) induced by the ultrasound probe. After the cells were incubated in adhesive films for various time points, the assays were carried out.

2.7. Effect of ultrasound-induced piezoelectric stimulation on macrophage polarization

Firstly, THP-1 seeded on adhesive films and incubated with PMA for 48 h. Then, to induce M1 and M2 polarization, M0 macrophage on adhesive films was cultured with stimulating factors-1 (SF1; 100 ng/mL LPS and 20 ng/mL IFN- γ) and stimulating factors-2 (SF2; 20 ng/mL IL-4 and 20 ng/mL IL-13) with or without ultrasound for 3 days, respectively. Flow cytometry was carried out to detect the biomarker (CD86 and CD206) of macrophages. Real-time quantitative polymerase chain reaction (RT-qPCR) was used to assess the relative gene expression of M1 and M2 macrophages. Immunofluorescence was performed to evaluate the relative marker expression of M1 and M2 macrophages (chemokine (C-C motif) receptor 7 (CCR7) and arginase-1 (Arg-1)). Furthermore, the relative semi-quantitative analysis was carried out by ImageJ software. The detailed information about antibodies and gene sequences is provided in Table S1 and Table S2 (Supporting Information).

2.8. Impact of ultrasound-induced piezoelectric stimulation on human rotator cuff tear tissue

The collection of supraspinatus tendon samples was approved by the Ethics Committee of Shanghai General Hospital, and informed consent was obtained from all participants (2022KY014C23-1). Samples of human-injured supraspinatus tendon were harvested from arthroscopic RCR, which were then cut into $\approx 3 \times 3 \times 4$ mm segments (four per sample) and placed on the adhesive films in a well plate with or without 5 min/day ultrasound stimulation. After a 3-day co-culture, the samples were collected and prepared into sections for subsequent inducible nitric oxide synthase (iNOS), CD68, and CD206 immunofluorescence staining. Detailed information about the antibodies is provided in Table S1 (Supporting Information).

2.9. Mechanisms of macrophages treated with ultrasound-induced piezoelectric stimulation

RNA sequencing analysis was employed to detect the gene expression changes between SF1-stimulated and SF1+N/P/M + US-stimulated macrophages. Trizol reagent (Invitrogen) was used to extract total RNA. RNA sequencing analysis was conducted by Shanghai Xu Ran Biotech (Shanghai, China). Data analysis was carried out on the cloud platform. A significant threshold was defined as a fold change exceeding 1.5 accompanied by a p-value below 0.05. Intracellular Ca²⁺ of THP-1 was detected using Fluo-4 AM (Beyotime, China). In detail, THP-1 was seeded on adhesive films and then serum-starved for 12 h. Subsequently, to inhibit TRPV1, THP-1 was incubated with 100 μ M AMG9810 (MedChemExpress, USA) for 2 h. After that, THP-1 was incubated with Fluo-4 AM in serum-free medium for 30 min. At the Ca²⁺-free medium, THP-1 was treated with or without CaCl₂ (2 mM) for 30 and 60 min, respectively. The images were measured by DMI8 microscope. The expression levels of phosphorylated protein kinase A (p-PKA), PKA, phosphorylated cAMP response element-binding protein (p-CREB), CREB were detected by western blotting. Enzyme-linked Immunosorbent Assay (ELISA), RT-qPCR, and immunofluorescence were further used to evaluate the inflammation levels after TRPV1 inhibition. The relative antibodies and RT-qPCR primers are provided in Table S1 and Table S2 (Supporting Information).

2.10. Effect of ultrasound-induced piezoelectric stimulation on HUVECs directly and in M1 conditioned medium

HUVECs were seeded on adhesive films and treated with or without ultrasound stimulation for 24 h. RT-qPCR and immunofluorescence were performed to assess the relative protein (VEGF) and gene expression (VEGF and α -SMA). Furthermore, M0 macrophages were seeded on adhesive films and incubated with or without SF1 and ultrasound stimulation for 3 days. The supernatants from different groups were obtained. The various conditioned medium (CM) was then prepared by mixing the supernatants and fresh ECM at a 1:1 ratio (M0 CM, M1 CM, M1+US CM, M1+N/P/M CM, and M1+N/P/M + US CM). The scratch and transwell tests were used to assess the migration ability of HUVECs under different CMs. The immunofluorescence, RT-qPCR and tube formation experiments were carried to evaluate angiogenic ability of HUVECs. For tube formation assay, HUVECs were seeded on matrigel matrix (Corning, USA) in a 48-well plate with different CMs for 6 h. The tubes were observed by DMI8 microscope (Leica, Germany) and measured using Image J software. The antibodies and gene sequences are provided in Table S1 and Table S2 (Supporting Information).

2.11. Animal models

The animal study was approved by the Institutional Animal Care and Use Committee of Shanghai General Hospital (AD2024090). A total of 78 female Sprague-Dawley (SD) rats (250 \pm 20 g) underwent RCR, conducted as follows: The rats were anesthetized using inhalation of isoflurane. The insertion point of supraspinatus tendon was exposed and bilaterally resected from the greater tuberosity of the humerus, and a bone tunnel was prepared at the greater tuberosity using a 0.5 mm diameter drill bit. A 4-0 suture was used to reattach the supraspinatus tendon to the greater tuberosity through the bone tunnel, and N/P/M adhesive films were applied at the tendon-to-bone interface. The surgical site was closed layer by layer, and the rats were treated with penicillin postoperatively. Three rats were designated as the sham group, where bilateral tendons were only tendon exposed without further treatment. Three rats underwent unilateral adhesive intervention, with the contralateral side serving as a non-intervention control. The rats requiring ultrasound treatment were subjected to daily ultrasound intervention (5 min) for two weeks post-surgery. All rats were euthanized using carbon dioxide inhalation. Samples were harvested

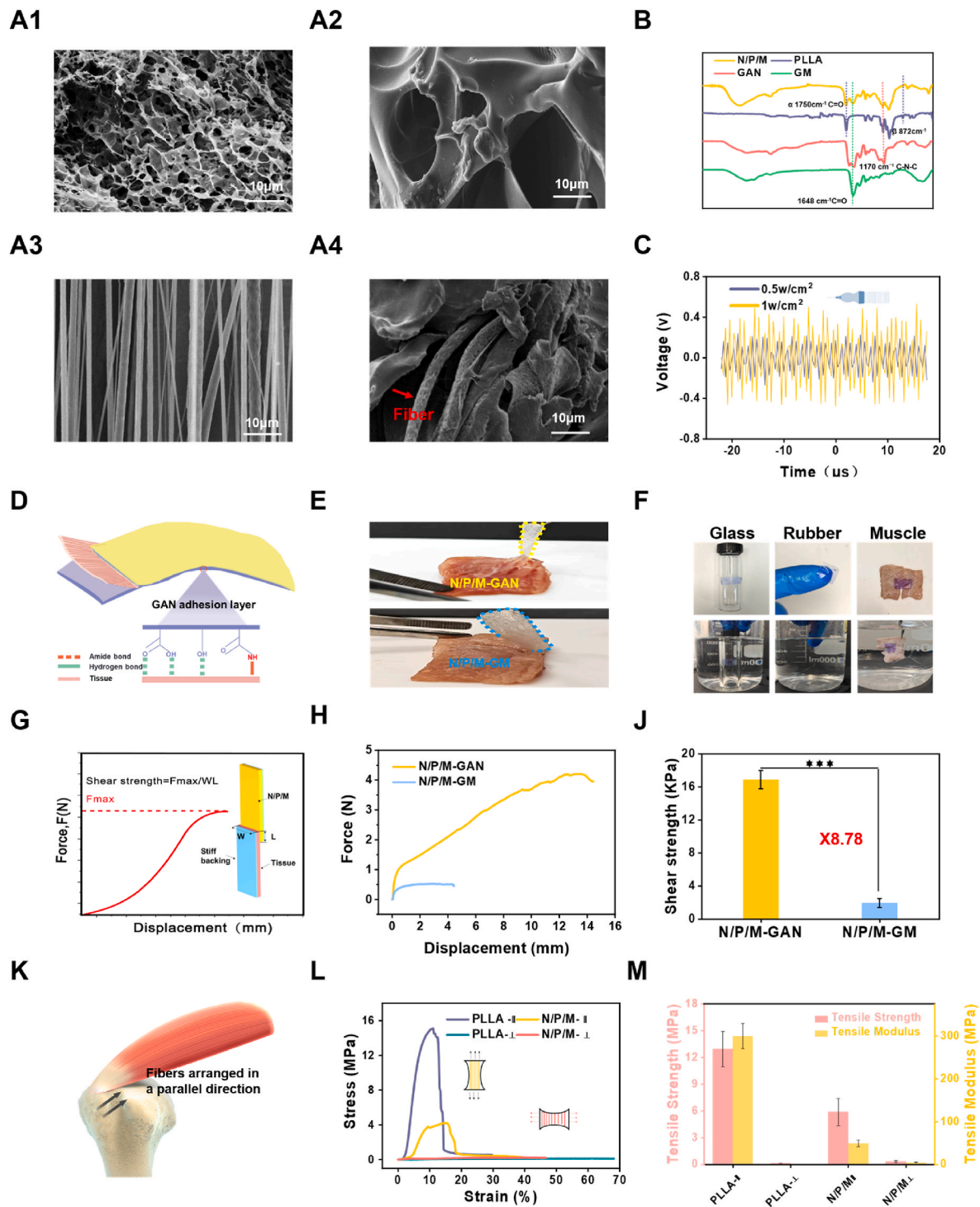


Fig. 1. Characterization of the physicochemical properties of N/P/M Janus adhesive films. A) SEM images of various samples: A1) GM hydrogel, A2) GAN hydrogel, A3) PLLA nanofiber membrane, and A4) N/P/M (red arrows indicated fibers). B) The FTIR spectra of N/P/M, PLLA, GAN, and GM. C) The representative output voltage waveforms of N/P/M sensor at 1 MHz frequency under US. D) The adhesion mechanism of N/P/M. E) The photographs of N/P/M adhering to pork tissue, demonstrating Janus asymmetric adhesion effects with GAN as the adhesive surface and GM as the non-adhesive surface. F) The images of N/P/M adhering to glass, rubber, and muscle surfaces both in the air and under water. G) The scheme of the lap-shear test setup. H) The shear force versus displacement curves for the N/P/M-GAN layer and the N/P/M-GM layer. J) The shear strength of the N/P/M-GAN layer and N/P/M-GM. K) The scheme of rotator cuff tendon, where collagen fibers are aligned in the direction indicated by the arrow. L) The stress-strain curves of PLLA and N/P/M along both parallel and perpendicular directions relative to fiber alignment. M) The tensile modulus and ultimate tensile strength (UTS) of PLLA and N/P/M along both parallel and perpendicular directions relative to fiber alignment. n = 5. *p < 0.05, **p < 0.01, and ***p < 0.001.

from these rats at one week postoperatively for proteomic analysis. Proteomic analysis was conducted by Genechem Biotechnology Co., Ltd. (Shanghai, China). The remaining 72 rats were divided into four groups: Control group, US group, N/P/M group, and N/P/M + US group. Each group consisted of 18 rats, which were euthanized at postoperative weeks 1, 2, 4, and 8 for histological analysis and biomechanical studies ($n = 6$).

2.12. Histological, immunohistochemical, and immunofluorescence analysis

The supraspinatus tendon-humeral complex was harvested and subsequently fixed in 4 % paraformaldehyde. After that, the complex was then subjected to decalcification with 10 % ethylenediaminetetraacetic acid (EDTA; Servicebio, China) for 3 weeks. The supraspinatus tendon-humeral complex was then sectioned into 5 μm slices and subjected to H&E, Toluidine Blue, picrosirius red and Safranin O-fast green staining; additionally, immunofluorescence staining for CD86, CD206, TNF- α , IL-10, Cox-2, VEGF, and α -SMA was performed, as well as immunohistochemical staining for types I, II, and III collagen. The histological scoring system was employed to evaluate the maturation of the supraspinatus tendon-humeral complex [11b]. (Table S3; Supporting Information). For, biosafety evaluation, the major organs (heart, lungs, spleen, liver, and kidneys) of rats in each group were harvested at eight weeks post-surgery, fixed with paraformaldehyde (PFA), and subsequently sectioned for H&E staining. Semi-quantitative analysis of the staining was conducted using Image J software. The antibody information is provided in Table S1 (Supporting Information).

2.13. Micro-CT analysis and biomechanical testing

The supraspinatus-humerus complex was subjected to Micro-CT (Bruker, USA) scanning with scanning parameters set to 90 kV and 270 mA. The region of interest included the tendon-to-bone interface and the greater tuberosity. Analysis parameters included bone volume to total volume ratio (BV/TV), trabecular number (Tb. N), trabecular thickness (Tb.th), and trabecular separation (Tb.sp). The cross-sectional area of the tendon at the tendon-to-bone interface was measured using a digital caliper. Biomechanical testing was performed using a universal testing machine (Instron 5567, USA). In brief, the humerus was fixed with a clamp, and the tendon was secured on the opposite side. Samples were loaded to failure using a pre-treatment force of 0.1 N and a loading rate of 10 mm/min [21]. The ultimate failure load, stress, and stiffness were recorded and analyzed.

2.14. Statistical analysis

Data analysis was performed using GraphPad Prism 8.0. Statistical analysis was conducted using Student's t-test or one-way analysis of variance (ANOVA). Results are presented as mean \pm standard deviation. A p-value of less than 0.05 was considered to indicate statistical significance.

3. Results and discussion

3.1. Synthesis and characterization of N/P/M Janus adhesive films

SEM images of the samples were shown in Fig. 1A, illustrating that both GAN and GM exhibited porous structures (Fig. 1A1 and 1A2). The electrospun PLLA nanofiber membranes, collected using a high-speed drum, possessing an oriented structure that mimicked the alignment of collagen fibers in natural tendons. Upon integration with hydrogels, these membranes formed an interpenetrating fibrous-hydrogel network (Fig. 1A3 and 1A4). This composite structure not only significantly improved the mechanical properties of the materials, but also created a more biocompatible environment. Such an environment was conducive

to guiding cell alignment and promoting tissue regeneration. As shown in Fig. 1B, the FTIR spectra of the PLLA nanofiber membrane and N/P/M adhesive films exhibited the characteristic peaks at 1750 cm^{-1} and 872 cm^{-1} , corresponding to the C=O stretching vibration of α -crystals and the β -phase peak, respectively. The results indicated that the PLLA nanofibers prepared by electrospinning formed an ordered crystalline phase, which was typically associated with piezoelectric properties. Additionally, N/P/M showed the characteristic peaks at 1648 cm^{-1} and 1170 cm^{-1} , attributed to the C=O stretching vibration of acrylamide and the symmetric stretching of the C-N-C bond in NHS groups, indicating successful integration of GAN and GM hydrogels with PLLA nanofibers. DSC data revealed that PLLA formed an ordered crystalline structure with a crystallinity of 44.7 %, further confirming the presence of piezoelectric properties (Fig. S1, Supporting Information) [22]. Compared to traditional pressure-induced electrical signal generation, the piezoelectric stimulation method using a handheld ultrasound device offered significant advantages. Its portability and ease of use made clinical applications more convenient, and simply placing the ultrasound transducer on the target area ensured stable and consistent electrical signals. As shown in Fig. 1C, the results showed the representative output voltage waveform of the N/P/M sensor at 1 MHz frequency using a handheld ultrasound device. Under different ultrasound power conditions, the N/P/M sensor consistently generated clear piezoelectric signals with uniform intervals and peak amplitudes. Specifically, at an ultrasound power of 1 W/cm^2 , the output voltage was approximately 404 mV; at 0.5 W/cm^2 , it was approximately 230 mV (Fig. S2, Supporting Information). We selected these two power levels to test the piezoelectric properties of this adhesive film, given that low-intensity ultrasound is generally regarded as safe for human applications [13b,23]. As shown in Fig. 1D, in the GAN adhesive layer, hydrogen bonds originate from Polyacrylic acid (PAA) (carboxyl and hydroxyl groups) and gelatin (hydroxyl groups) interacting with the tissue surface, providing rapid initial adhesion. Simultaneously, NHS esters react with amino groups on the tissue surface to form stable amide bonds, ensuring long-term adhesion. This unique chemical design enables the GAN layer to adhere firmly to soft tissues, a capability that the GM layer lacks, thereby demonstrating the Janus effect of the N/P/M adhesive films (Fig. 1E). Further validation showed that the N/P/M adhesive films exhibited robust adhesion not only in air but also under water, adhering strongly to various surfaces such as muscle, glass, and rubber (Fig. 1F). This property was particularly significant for rotator cuff tissue, which were rich in fluids like synovial fluid and tissue fluid. The exceptional adhesion capability of N/P/M ensured stability and functionality even in complex biological environments filled with liquids.

Quantitative characterization of the adhesion performance according to ASTM F2255 lap shear test standards (Fig. 1G) revealed that the shear force of the GAN layer significantly exceeded that of the GM layer (Fig. 1H). Specifically, the shear strength of the GAN layer reached $16.86 \pm 1.11\text{ KPa}$, approximately 8.78 times higher than that of the GM layer ($1.92 \pm 0.55\text{ KPa}$), and surpassed the performance of commercially available cyanoacrylate adhesives reported in the literature [22c] (Fig. 1J). Moreover, N/P/M exhibited excellent flexibility and elasticity, enabling it to bend and twist, which made it well-suited for the demanding environment of the rotator cuff (Fig. S3, Supporting Information). Therefore, the Janus adhesion effect exhibited by N/P/M not only provided superior adhesion performance but also offered several clinical advantages: it eliminated the need for surgical suturing and prevented unnecessary adhesion to surrounding normal tissues. These characteristics simplified the surgical process, reduced operative time and patient discomfort, minimized postoperative complications, and promoted faster recovery and functional restoration [22c]. Natural tendons exhibited mechanical anisotropy, with collagen fiber bundles aligned in the direction indicated by the arrow, providing excellent mechanical properties to the tendon tissue (Fig. 1K) [11b,24]. To evaluate the mechanical anisotropy of the piezoelectric nanofiber membrane

and composites, tensile tests were conducted in both parallel and perpendicular directions relative to the fiber alignment (Fig. 1L). The stress-strain curves revealed that, for both PLLA and N/P/M, the tensile strength in the parallel direction was significantly higher than in the perpendicular direction. This anisotropic behavior was attributed to the oriented structure of the PLLA nanofibers, which was preserved when combined with the hydrogel, enhancing the mechanical performance in the parallel direction [21,25]. The parallel tensile strength of N/P/M reached 5.88 ± 1.53 MPa, with a modulus of 48.85 ± 7.37 MPa and an elongation at break of 13.21 ± 2.28 % (Fig. 1M and Fig. S4, Supporting Information), closely matching the mechanical properties of human rotator cuff tendons, which have a tensile strength of 5–100 MPa, a Young's modulus of 20–1200 MPa, and an elongation at break of 10–15 % [24]. This structural biomimetic design not only replicated the natural anisotropy of tendon tissues but also achieved similar mechanical properties. In summary, the N/P/M adhesive films exhibited stable piezoelectric properties, unique Janus adhesion effects, biomimetic anisotropy, and mechanical properties similar to those of human tendons. These characteristics ensured the stability and functionality in complex biological environments, providing an innovative and clinically advantageous solution for rotator cuff injury repair.

3.2. Ultrasound-induced piezoelectric stimulation regulated macrophage polarization

The CCK-8 and live/dead staining assays demonstrated that N/P/M exhibited good cell compatibility when co-cultured with HUVECs for 5 days and with THP-1 for 3 days, under 0.5 W/cm^2 and 1 W/cm^2 ultrasound intensity (Figs. S5–6, Supporting Information). We investigated the impact of different interventions on macrophage polarization. As shown in Fig. 2A–H, immunofluorescence and flow cytometry results indicated that macrophages stimulated with SF1 or SF2 exhibited a significant increase in the expression of the biomarker of M1 phenotype (CCR7 and CD86), or the biomarker of M2 phenotype (Arg-1 and CD206), respectively. In comparison, the expression of CCR7 and CD86 was significantly downregulated in the SF1+US (1 W/cm^2) + N/P/M group, while the expression of Arg-1 and CD206 was further significantly upregulated in the SF2+US (1 W/cm^2) + N/P/M group. However, when US (1 W/cm^2) or N/P/M was used individually to treat macrophages stimulated with SF1 or SF2, there was no significant alteration in the expression of CCR7, CD86, CD206, and Arg-1.

Similar results were also obtained through the analysis of the inflammatory gene expression levels using RT-qPCR. The combined intervention of US (1 W/cm^2) with N/P/M significantly suppressed the expression of pro-inflammatory genes in SF1-stimulated macrophages (*TNF- α* , *IL-6*, *IL-1 β*), while further significantly promoting the anti-inflammatory genes expression in SF2-stimulated macrophages (*Arg-1*, *IL-10*, *IL-1ra*) (Fig. 2J and K). Nonetheless, the application of US (1 W/cm^2) or N/P/M in isolation to macrophages activated by SF1 or SF2 did not result in any significant modulation of the pro-inflammatory or anti-inflammatory genes expression levels. Previous studies were reported that low-intensity pulse stimulation (LIPUS) might exhibit anti-inflammatory effects, which is inconsistent with the results of this study [26]. Further analysis revealed that the reported ultrasound intensity was tens of mV/cm^2 , which significantly differs from the ultrasound intensity used to drive the piezoelectric stimulation in this study. This might be the reason for the different inflammatory regulatory effects observed.

To further explore the ability of N/P/M to modulate macrophages under different ultrasound intensity, we selected 0.5 W/cm^2 and 1 W/cm^2 for the following experiments. As indicated in Figs. S7–10, Supporting Information, immunofluorescence and flow cytometry results demonstrated that both 0.5 W/cm^2 and 1 W/cm^2 driven N/P/M significantly downregulated the expression of CD86 and CCR7 in SF1-treated macrophages, while upregulating the expression of CD206 and Arg-1 in macrophages stimulated by SF2. However, compared to the SF1 or SF2

groups, N/P/M under 1 W/cm^2 indicated more significant differences than 0.5 W/cm^2 . The results of RT-qPCR further substantiated this phenomenon (Fig. S11, Supporting Information). N/P/M under 1 W/cm^2 showed a greater capacity to inhibit the expression of pro-inflammatory genes and upregulate the anti-inflammatory genes expression compared to those under 0.5 W/cm^2 .

3.3. Ultrasound-induced piezoelectric stimulation regulated macrophage polarization in human-injured rotator cuff specimens

To further investigate the anti-inflammatory properties of N/P/M under US, immunofluorescence double-staining of human-injured rotator cuff samples revealed that N/P/M under 1 W/cm^2 significantly reduced iNOS intensity within the tissue, while significantly enhancing the expression of CD206. However, neither US nor N/P/M alone showed a notable alteration in the expression levels of iNOS and CD206 (Fig. 2L). Subsequent semi-quantitative analysis confirmed that N/P/M at 1 W/cm^2 markedly decreased the proportion of iNOS and increased the expression ratio of CD206 in the injured tissue (Fig. S12, Supporting Information). In summary, these results demonstrated that N/P/M driven by ultrasound possessed superior capability to modulate inflammation *in vitro* and *ex vivo*.

3.4. Ultrasound-induced piezoelectric stimulation inhibited M1 macrophage polarization in the TRPV1/ Ca^{2+} /cAMP manner

We further explored the underlying mechanisms by which ultrasound-induced piezoelectric stimulation suppressed M1 macrophages polarization. Specifically, we conducted RNA sequencing on SF1-treated macrophages and SF1-treated macrophages intervened by US + N/P/M, and the group of SF1-treated macrophages was set as the control group. Initially, principal component analysis (PCA) results highlighted substantial variations in RNA expression between the two groups (Fig. S13, Supporting Information). Subsequent heatmap and volcano plot analyses revealed that, compared to the SF1 group, the SF1+US + N/P/M group exhibited 462 upregulated genes and 329 downregulated genes (Fig. 3A; Fig. S14, Supporting Information). The results of Gene Ontology (GO) enrichment analysis revealed that the differential genes were primarily related to immune responses, ion transmembrane transport, and mitochondrial activity (Fig. 3B). Further KEGG analysis indicated that these differential genes were associated with Inflammatory mediator regulation of TRP channels and cyclic adenosine monophosphate (cAMP) pathways (Fig. 3C). Gene Set Enrichment Analysis (GSEA) demonstrated that, compared to the SF1 group, the SF1+US + N/P/M group upregulated Inflammatory mediator regulation of TRP channels and cAMP signaling pathways (Fig. 3D).

The transient receptor potential ion channels are multifunctional signaling molecules, which are closely associated with a variety of physiological and pathological processes [27]. They can respond to stimuli such as temperature, pressure, and electricity, and are responsible for the ion translocation (Ca^{2+}). Furthermore, they are widely distributed across various immune cell types [28]. Transient receptor potential vanilloid 1 (TRPV1), one of the representative cation channels, is involved in inflammation progress and pain perception. Recent study was reported that the activation of TRPV1 can reduce the inflammatory mediator expression through Ca^{2+} /CaMKII/nuclear factor erythroid 2-related factor 2 (NRF2) signaling pathway, thereby inhibiting M1 macrophages polarization [29]. Consequently, we conducted an in-depth GO analysis, which demonstrated multiple GO terms enrichment associated with Ca^{2+} transport among the differential genes (Fig. 3E). Furthermore, the TRPV1 gene was also found to be significantly upregulated among the differentially expressed genes. In addition, the cAMP signaling pathway, a classic anti-inflammatory pathway, was reported to be activated by Ca^{2+} (important second messenger), further exerting the anti-inflammatory functions [30]. Therefore, we hypothesized that in this study, ultrasound-induced piezoelectric

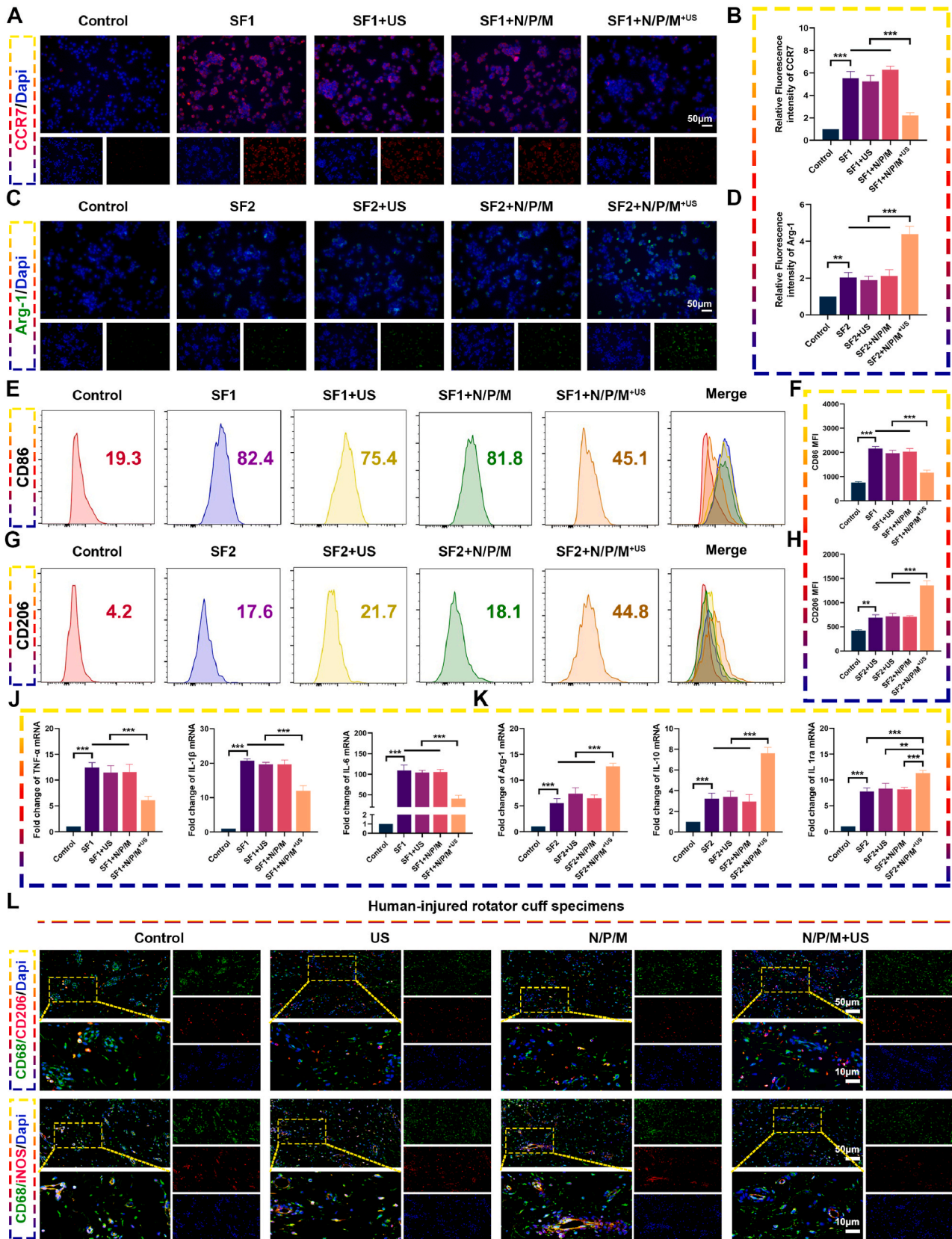


Fig. 2. Ultrasound-induced piezoelectric stimulation modulated macrophage polarization *in vitro* and in human-injured rotator cuff specimens. A-D) Immunofluorescence and its semi-quantitative analysis of macrophage-related proteins (M1: CCR7; M2: Arg-1) (n = 3). E-H) Flow cytometry analysis of M1 macrophage-related protein (CD86) and M2 macrophage-related protein (CD206) (n = 3). J-K) RT-qPCR results of macrophage-related genes (M1: *TNF-α*, *IL-1β*, and *IL-6*; M2: *Arg-1*, *IL-10*, and *IL-1ra*) (n = 3). L) Immunofluorescence and its semi-quantitative analysis of iNOS and CD206 in human-injured rotator cuff specimens (n = 6). *p < 0.05, **p < 0.01, and ***p < 0.001.

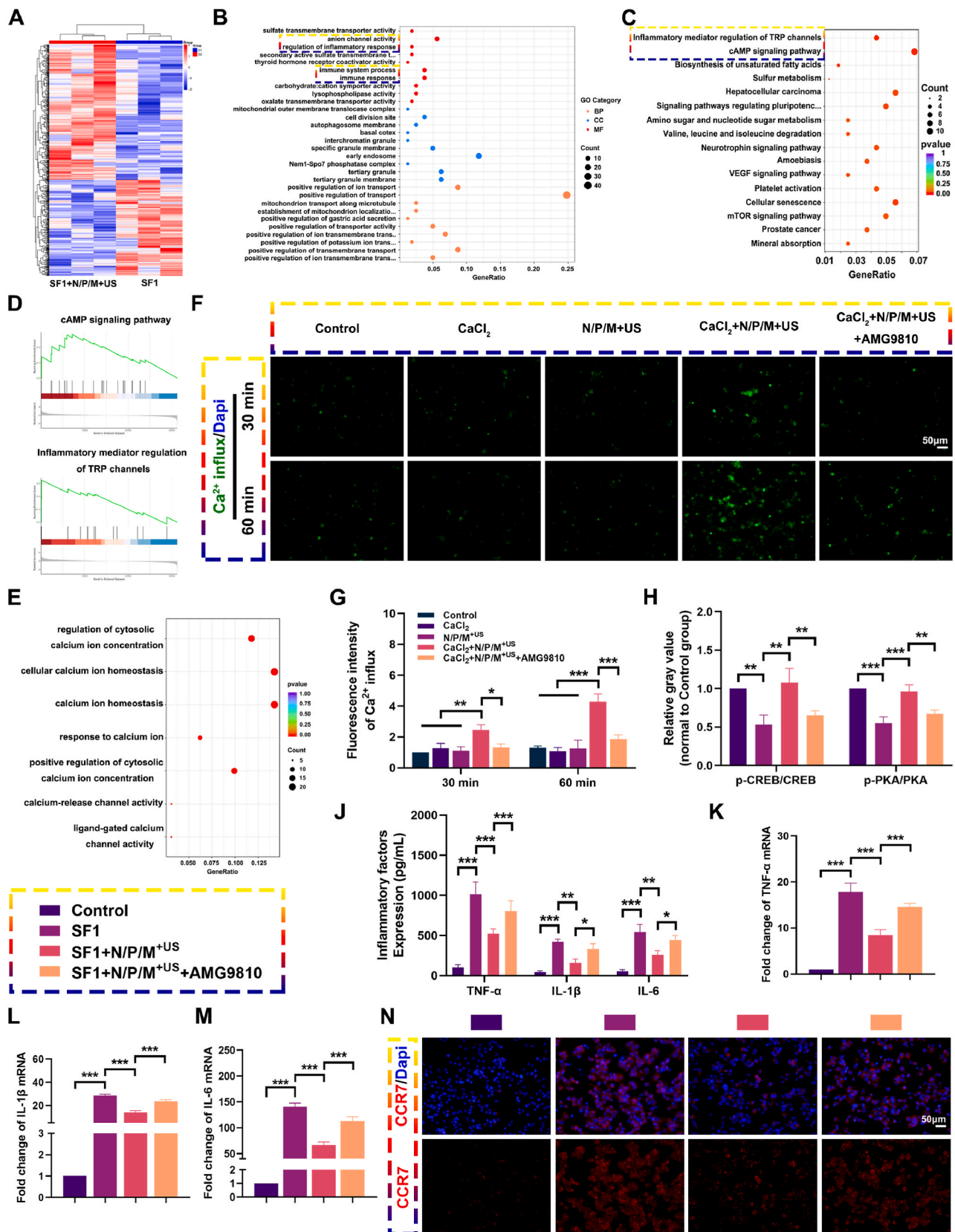


Fig. 3. Ultrasound-induced piezoelectric stimulation inhibited macrophage polarization towards M1 phenotype by activating TRPV1/ Ca^{2+} /CAMP axis. **A)** Heatmap analysis. **B)** GO enrichment analysis and KEGG pathway analysis. **D)** Gene set enrichment analysis. **E)** GO enrichment related to Ca^{2+} transport. **F-G)** Typical images of Ca^{2+} influx assays and corresponding semi-quantitative analysis ($n = 3$). **H)** Semi-quantitative analysis of p-CREB/CREB and p-PKA/PKA ($n = 3$). **J)** The inflammatory factors expression measured by ELISA ($n = 3$). **K-M)** RT-qPCR analysis of inflammation-related genes (*TNF- α* , *IL-1 β* , and *IL-6*) ($n = 3$). **N)** Typical images of CCR7 immunofluorescence ($n = 3$). * $p < 0.05$, ** $p < 0.01$, and *** $p < 0.001$.

stimulation facilitated the influx of Ca^{2+} by activating TRPV1, subsequently activating the cAMP signaling pathway, ultimately achieving an anti-inflammatory effect.

We initially utilized Fluo-4 AM (cell-permeable Ca^{2+} probe) to detect intracellular Ca^{2+} concentrations under Ca^{2+} -free conditions, in the presence or absence of US + N/P/M and CaCl_2 . Fluorescence results from co-culture periods of 30 min and 60 min demonstrated that no significant fluorescence intensity was observed in the control group, the CaCl_2 group, or the US + N/P/M group at both time points. However, the CaCl_2 +US + N/P/M group exhibited significant fluorescence intensity at both time points, with a notable increase in fluorescence intensity as time progressed. Furthermore, we utilized AMG9180 (the selective TRPV1 antagonist) in co-culture with CaCl_2 and US + N/P/M, and the results indicated a significant reduction in fluorescence intensity at both time points, compared to the CaCl_2 +US + N/P/M group. Corresponding semi-quantitative analysis also demonstrated consistent results (Fig. 3F and G). These results suggested that N/P/M under US can significantly promote Ca^{2+} influx, which was closely associated with TRPV1 activation. To further investigate the relationship between TRPV1 activation and cAMP signaling pathway, we examined the expression of proteins within this pathway in SF1-treated macrophages, with or without the intervention of US + N/P/M. The results revealed a significant upregulation of phosphorylated protein kinase A (p-PKA) and cAMP response element-binding protein (p-CREB) in the SF1+US + N/P/M group, whereas there were no significant alterations in PKA and CREB levels compared with the SF1 group. However, we observed that the presence of AMG9180 significantly diminished the ability of the SF1+N/P/M + US group to upregulate p-PKA and p-CREB. (Fig. 3H; Fig. S15, Supporting Information). Subsequently, ELISA, immunofluorescence, and RT-qPCR results indicated that N/P/M under US significantly downregulated the pro-inflammatory proteins and genes expression; however, in the presence of AMG9180, this downregulatory effect was significantly reversed (Fig. 3J–N; Fig. S16, Supporting Information). In summary, N/P/M under US can effectively activate TRPV1, promote Ca^{2+} influx, thereby activating the cAMP signaling pathway, and ultimately exert a superior anti-inflammatory effect.

3.5. Ultrasound-induced piezoelectric stimulation mitigated the inhibitory effects of M1 macrophages on HUVEC migration and angiogenesis

Considering that enhanced vascularization at the tendon-to-bone interface facilitates the supply of essential nutrients, thereby promoting tendon-to-bone enthesis repair, we further examined the effects of N/P/M under US on HUVEC angiogenesis [31]. We firstly explored the direct impact of N/P/M under US on the angiogenesis of HUVECs. Immunofluorescence and RT-qPCR results indicated that N/P/M at 1 W/cm² did not significantly affect the expression of VEGF protein and the angiogenesis-related genes (α -SMA and VEGF) expression levels in HUVECs (Figs. S17–18, Supporting Information). Subsequently, we collected the supernatant from SF1-treated macrophages with the intervention of US + N/P/M to explore the effects of ultrasound-induced piezoelectric stimulation on the migration and angiogenesis of HUVECs in the inflammatory environment (Fig. 4A). The results of the scratch and transwell assays demonstrated that, compared to the conditioned medium from M0 macrophages (M0 CM), the conditioned medium from M1 macrophages (M1 CM) significantly inhibited the migratory ability of HUVECs, with further semi-quantitative analysis yielding consistent results (Fig. 4B–E). In contrast, the US + N/P/M intervention had a significant alleviating effect on this inhibitory action, reaching levels comparable to those observed with M0 CM. However, neither US nor N/P/M alone could reverse this inhibitory effect. Immunofluorescence results indicated that M1 CM significantly suppressed the VEGF expression in HUVECs, whereas the US + N/P/M intervention significantly enhanced the expression of VEGF (Fig. 4F and G). On the contrary, US or N/P/M alone did not alleviate the suppressive effect of M1 CM on VEGF expression in HUVECs. Furthermore, the tube formation

assay results showed that M1 CM significantly inhibited the tubule forming capability of HUVECs compared to M0 CM. However, US + N/P/M significantly mitigated the inhibitory effects of M1 CM. Semi-quantitative analysis revealed that US + N/P/M effectively increased the total length, junctions and meshes numbers, which were reduced by M1 CM (Fig. 4H–L). Nevertheless, US or N/P/M alone did not increase the number of tubes suppressed by M1 CM. RT-qPCR results demonstrated that US + N/P/M significantly upregulated the expression levels of VEGF and α -SMA genes, which were suppressed by M1 CM (Fig. 4M and N). These results further substantiate the ability of US + N/P/M to preserve the angiogenic capacity of HUVECs in an inflammatory environment. Altogether, these findings demonstrated that N/P/M under US effectively mitigated the impairment of HUVEC migration and angiogenic capacity in an inflammatory environment.

3.6. Ultrasound-induced piezoelectric stimulation alleviated the inflammation at the tendon-to-bone enthesis in a time-dependent manner

Early inflammatory responses are the initiating factors for the fibrous scar tissue formation, which can have a significant negative impact on the healing of the enthesis. Extensive studies were indicated that inhibiting macrophages polarization towards M1 phenotype and promoting M2 phenotype can contribute to enhanced tendon-to-bone healing [31,32]. Based on the anti-inflammatory effects of N/P/M under US *in vitro* and *ex vivo*, we established a rat RCR model and adhered N/P/M to the injured site with US treatment to further observe its regulatory effects on early inflammation (Fig. 5A). N/P/M can be easily adhered to the tendon-to-bone interface, forming a tight adhesion without any additional fixation procedures, thereby greatly simplifying its clinical application (Video S1). Unlike some studies that assess inflammatory status at a single early postoperative time point, we conducted a sustained assessment of the inflammation during the first- and second-weeks post-surgery. This approach was employed to achieve a more comprehensive exploration on the effects of N/P/M under US [11b,21]. As shown in Fig. 5B and C, During the postoperative first week, immunofluorescence staining was performed for CD86 and TNF- α (M1 macrophage markers). The results revealed that the control group exhibited pronounced expression of CD86 and TNF- α . In contrast, the US + N/P/M group demonstrated a significant reduction in CD86 and TNF- α expression. However, both the US and N/P/M groups showed a significant elevation in CD86 and TNF- α expression, similar to that observed in the control group. By the second week postoperatively, the control, US, and N/P/M groups demonstrated a relative decrease in CD86 and TNF- α expression compared to the first postoperative week, yet still exhibited significant expression levels. Notably, the US + N/P/M group showed a further reduction in CD86 and TNF- α expression. Subsequently, the results of immunofluorescence for CD206 and IL-10 (M2 macrophage markers), revealed that the control group exhibited minimal expression of CD206 and IL-10 at the first week. Similarly, the US and N/P/M groups showed low levels of CD206 and IL-10 expression. In comparison, the US + N/P/M group demonstrated a notably higher expression of these markers (Fig. 5D and E). During the second week post-surgery, there was a slight increase in the expression of CD206 and IL-10 in the control, US, and N/P/M groups. In contrast, the US + N/P/M group exhibited a significant trend towards increased expression of CD206 and IL-10. Subsequent semi-quantitative analysis of immunofluorescence results also demonstrated a consistent trend for CD86, TNF- α , CD206, and IL-10 intensity (Fig. 5F; Fig. S19, Supporting Information). Altogether, through the dynamic assessment of inflammatory levels at two time points over two weeks postoperatively, we found that N/P/M under US continuously reduced the expression of M1 macrophage markers and promoted the expression of M2 macrophage markers, thereby providing substantial evidence for the effective anti-inflammatory action of US + N/P/M *in vivo*.

Supplementary video related to this article can be found at <https://doi.org/10.1016/j.ceramint.2025.02.045>

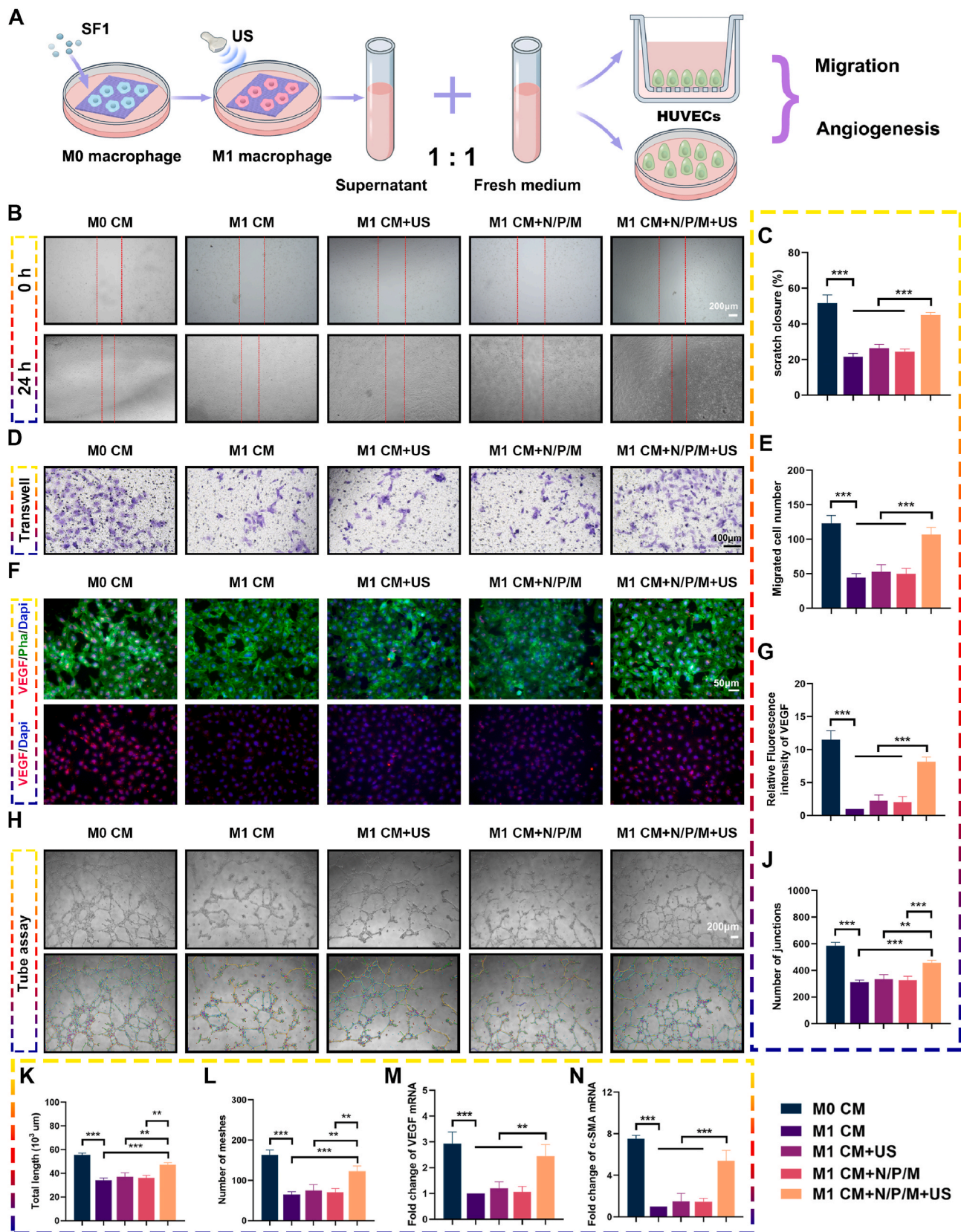


Fig. 4. Ultrasound-induced piezoelectric stimulation facilitated HUVEC migration and angiogenesis by alleviating the suppressive effects of the inflammatory microenvironment mediated by M1 macrophages. **A)** Illustrations depicting the influence of ultrasound-induced piezoelectric stimulation on HUVEC migration and angiogenesis within the M1 conditioned medium (CM) environment. SF1 represents 100 ng/mL LPS and 20 ng/mL IFN- γ . US represents ultrasound. **B-E)** Typical images and semi-quantitative assessments from the scratch and transwell assays ($n = 3$). **F-G)** Representative VEGF immunofluorescence images and the relative semi-quantitative analysis ($n = 3$). **H-L)** Representative images from tube formation assays and semi-quantitative analysis of junctions, total length, and meshes ($n = 3$). **M – N)** RT-qPCR analysis of angiogenesis-related genes (*VEGF* and α -SMA) ($n = 3$). * $p < 0.05$, ** $p < 0.01$, and *** $p < 0.001$.

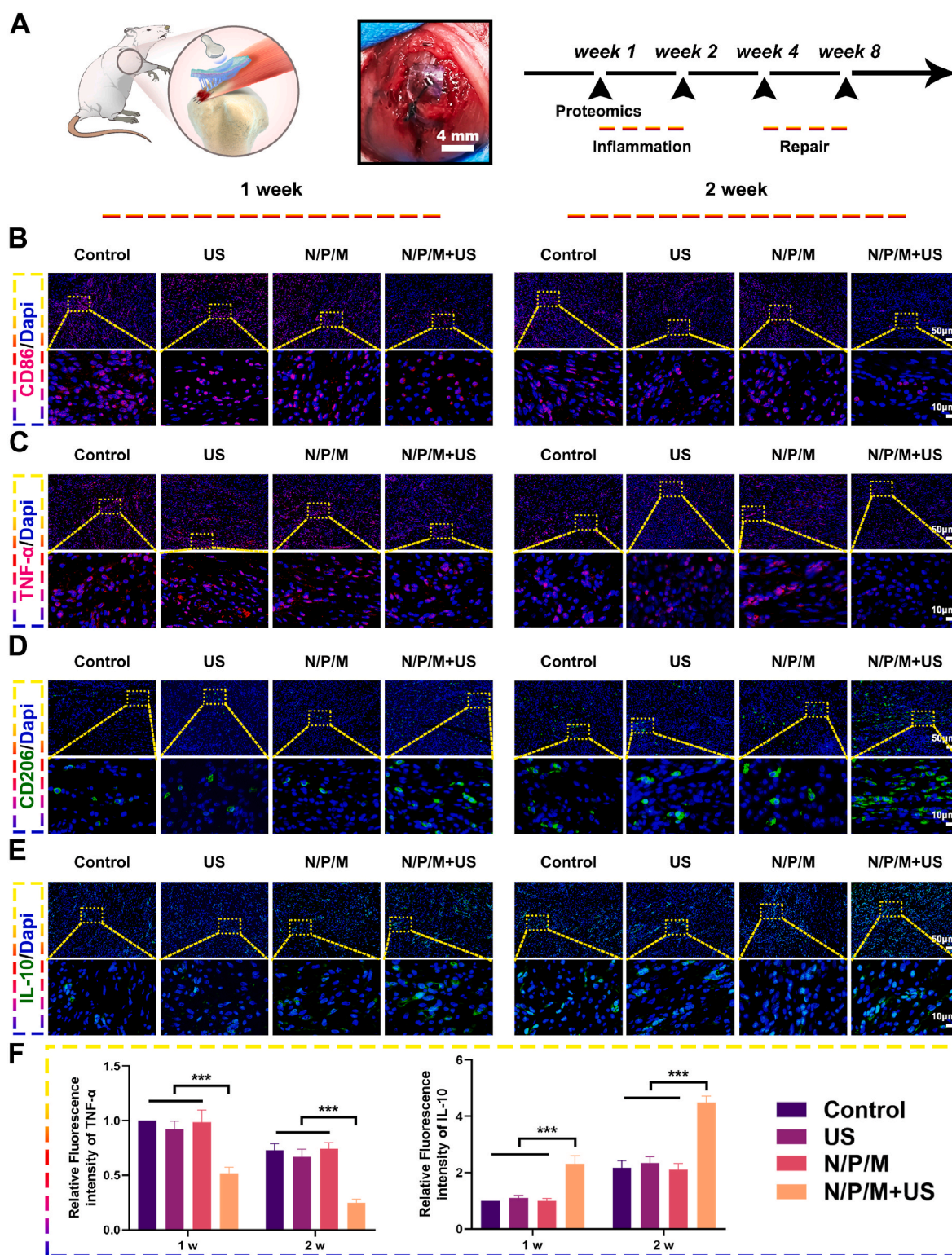


Fig. 5. Ultrasound-induced piezoelectric stimulation ameliorates the inflammatory microenvironment in a rat RCR model in a time-dependent manner. A) Illustrations depicting the process of N/P/M adhesion at the tendon-to-bone interface and the details of postoperative harvesting procedures. B-C) Typical immunofluorescence images of CD86 and TNF- α expression at the tendon-to-bone interface at 1 week and 2 weeks postoperatively. D-E) Representative immunofluorescence images of CD206 and IL-10 expression at the tendon-to-bone interface at 1 week and 2 weeks postoperatively. F) Semi-quantitative analysis of TNF- α and IL-10 at the tendon-to-bone interface at 1 week and 2 weeks postoperatively. $n = 6$. * $p < 0.05$, ** $p < 0.01$, and *** $p < 0.001$.

3.7. Proteomic analysis: early effects of ultrasound-induced piezoelectric stimulation on the tendon-to-bone enthesis

It should be highlighted that transcriptomics generally offers a

broader view of cellular alterations at the genomic level, albeit with less certainty, whereas proteomics delivers more dependable insights into cellular responses at the protein expression level, though with a less comprehensive scope [33]. Therefore, multi-omics, by integrating

transcriptomics and proteomics, allows for a synergistic approach to achieve a more holistic and dependable insight into the interactions between biomaterials and biological entities (cells and tissues). Recent studies were frequent reported to employ RNA sequencing or proteomic analysis to explore the interactions between cells and biomaterials [34].

However, there is a lack of systematic investigations examining the impact of piezoelectric stimulation on cells and tissues at both transcriptomic and proteomic dimensions. To further investigate the impact of N/P/M under US on the tendon-to-bone healing *in vivo*, we collected the enthesis samples from the two groups (the control group and the US

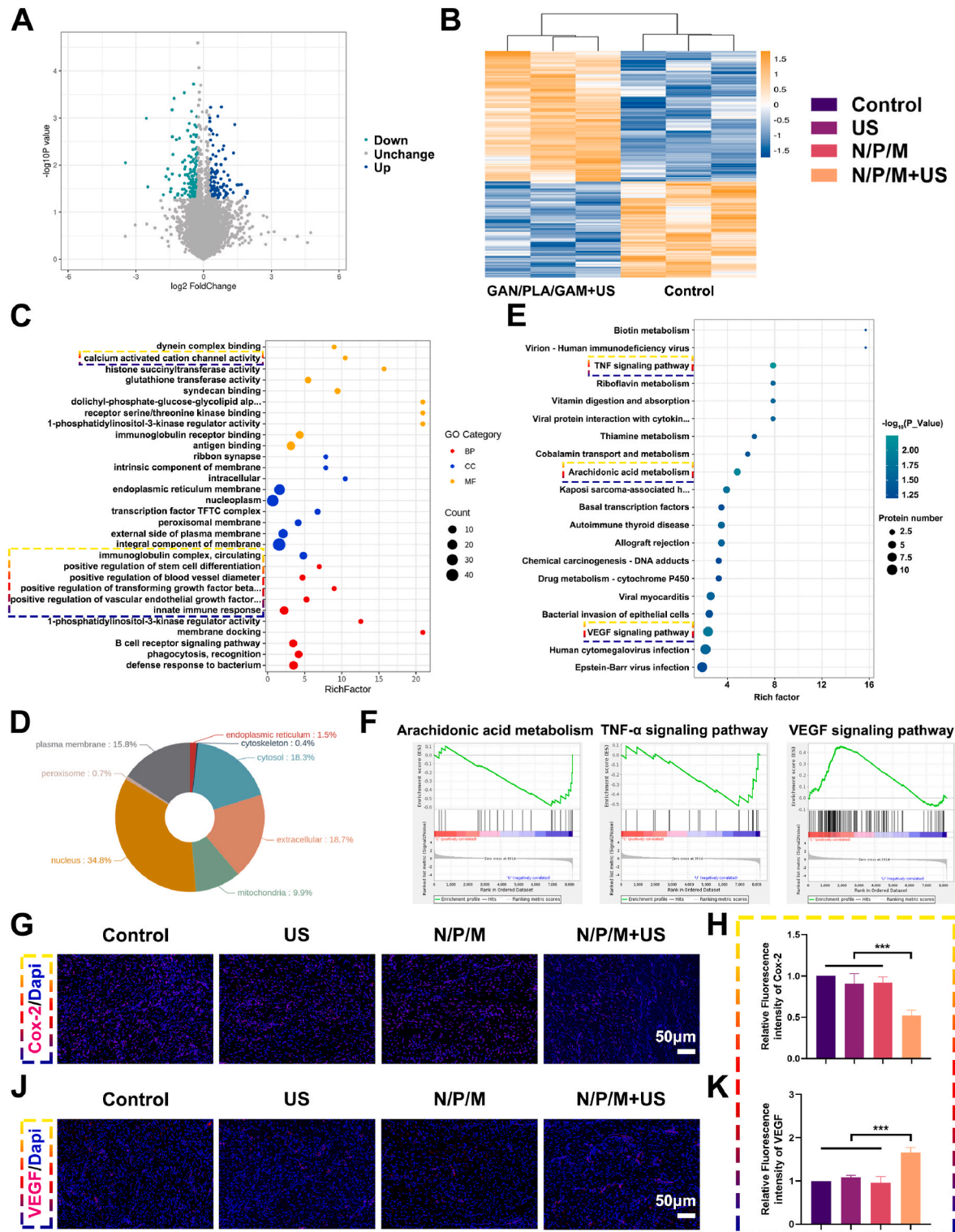


Fig. 6. Proteomic analysis of the tendon-to-bone interface following ultrasound-induced piezoelectric stimulation. A) Volcano plot analysis. B) Heatmap analysis. C) Top 30 GO enrichment analysis. D) Subcellular localization analysis of differentially expressed proteins. E) Top 20 GO enrichment analysis. F) Gene set enrichment analysis. G-K) Typical immunofluorescence images of Cox-2 and VEGF expression at the tendon-to-bone interface at 1 week postoperatively. $n = 6$. * $p < 0.05$, ** $p < 0.01$, and *** $p < 0.001$.

+ N/P/M group) at the first postoperative week for proteomic analysis. PCA results revealed significant differences in protein expression between the two groups (Fig. S20, Supporting Information). Further analysis identified 273 differentially expressed proteins in the US + N/P/M group compared to the control group, with 116 proteins being significantly upregulated and 157 proteins being significantly downregulated (Fig. 6A and B). GO enrichment analysis indicated that the differential protein expression was predominantly associated with immune responses, angiogenesis events, calcium ion channel activity, and positive regulation of stem cell differentiation (Fig. 6C). Subcellular localization results indicated that the differentially expressed proteins were predominantly localized to the nucleus and the extracellular compartment (Fig. 6D). KEGG analysis demonstrated that the differentially expressed proteins were associated with multiple signaling pathways, including Arachidonic acid (ArA) metabolism, TNF- α signaling pathway, and VEGF signaling pathway (Fig. 6E). In detail, ArA metabolism and its downstream prostaglandins product are potent pro-inflammatory factors, significantly impacting the repair of musculoskeletal system injuries [35]. Free ArA undergoes metabolic conversion to Prostaglandin E2 (PGE2) via the cyclooxygenase (COX) pathway. Subsequently, The PGE2 generated by COX-2 serves to amplify and prolong the inflammatory response [36]. We also observed down-regulation of PGE2 among the differentially expressed proteins. The inhibition of ArA metabolism and TNF- α signaling pathway might be closely associated with the anti-inflammatory effects of N/P/M under US. Interestingly, we observed a significant upregulation of VEGF signaling pathway, which is consistent with the macrophage RNA sequencing results, suggesting that N/P/M under US might promote macrophages polarization towards M2 phenotype, leading to the secretion of factors conducive to angiogenesis and thereby facilitating vascular regeneration at the tissue level. Stahl et al. demonstrated that tailored graft pore sizes directly promoted M2 macrophage polarization, which enhanced VEGF secretion and angiogenesis via IL-10/STAT3 signaling [37]. Huang et al. reported that Cobalt-loaded PCL grafts regulated M2 macrophages to amplify VEGF-driven endothelial migration and nitric oxide production to promote angiogenesis [38]. GSEA results further demonstrated that, compared to the Control group, the N/P/M + US group upregulated VEGF signaling pathway and down-regulated ArA metabolism and TNF- α signaling pathways (Fig. 6F). To further validate these findings, we performed immunofluorescence staining for COX-2 and VEGF at the tendon-to-bone interface. The results demonstrated that the control, US, and N/P/M groups exhibited high expression of COX-2 and low VEGF expression. In contrast, the US + N/P/M group showed a significant decrease in COX-2 expression and a significant increase in VEGF expression (Fig. 6G–K). In summary, proteomic analysis of the tissue further elucidates the underlying mechanisms by which N/P/M under US achieves anti-inflammatory effects and promotes angiogenesis *in vivo*.

3.8. Ultrasound-induced piezoelectric stimulation promoted the tendon-to-bone enthesis repair

The tendon-to-bone enthesis is naturally constituted by four gradient layers: bone, mineralized fibrocartilage, unmineralized fibrocartilage, and tendon. The advantage of this structure lies in the capacity to minimize stress concentration and effectively distribute the load across the skeletal system [39]. The alleviation of inflammation serves as an effective prerequisite for facilitating tendon-to-bone interface repair, which is conducive to the remodeling of the fibrocartilaginous layer at the tendon-to-bone enthesis. Therefore, we firstly employed H&E staining to assess the repair of the supraspinatus tendon. At 4 weeks postoperatively, the results indicated that the tendon-to-bone interface structure was relatively disordered in the control, US, and N/P/M groups, while it was more organized in the US + N/P/M group. By the eighth week postoperatively, the tendon-to-bone interface structure in all groups had further improved in organization compared to the fourth

week, with the US + N/P/M group demonstrating the most orderly state (Fig. 7A). The histological scoring results demonstrated a gradual increase across all groups from 4 to 8 weeks postoperatively. At both 4 and 8 weeks postoperatively, the histological scores were similar in the control group, US group, and N/P/M group. In contrast, the US + N/P/M group exhibited significantly higher histological scores compared to the other groups (Fig. 7F). These findings indicated that N/P/M under US significantly enhanced the alignment, integrity, and maturation of the regenerated tendon-to-bone interface, which are crucial for maintaining good long-term function post-surgery. Picrosirius red staining was further employed to assess the repair efficacy and maturity of the regenerated tendon, wherein collagen I is manifested as yellow or red, and collagen III appears as green (Fig. 7B). At four weeks postoperatively, the control group, US group, and N/P/M group all exhibited high levels of collagen type III and low levels of collagen type I. In contrast, the US + N/P/M group displayed a higher proportion of collagen I and lower levels of collagen III. By the eighth week postoperatively, collagen maturity increased further in all groups; in addition, the US + N/P/M group continued to demonstrate the highest collagen I level and the lowest collagen III level. Additional immunohistochemical staining for collagen I and collagen III also revealed that the US + N/P/M group had the highest content of collagen I and the lowest content of collagen III in the supraspinatus tendon at both 4 and 8 weeks (Fig. 7C; Fig. S21, Supporting Information). Further semi-quantitative analysis of immunohistochemical staining also revealed a consistent trend (Fig. S22, Supporting Information). Masson's trichrome staining results at two time points indicated that the US + N/P/M group exhibited a higher collagen fiber content compared to the other three groups, with no significant differences in collagen fiber content observed among the remaining groups (Fig. S23, Supporting Information). In addition, the results of various staining for the sham group were depicted in Fig. S24, Supporting Information.

Subsequently, we employed Safranin O-fast green staining, collagen II immunohistochemical staining, and Toluidine Blue staining to further assess the formation of fibrocartilage at the tendon-to-bone interface. Proteoglycans in the regenerated tissue were stained red by Safranin O and blue by Toluidine Blue, respectively. At 4 weeks postoperatively, fibrocartilage regeneration was scant in the control, US, and N/P/M groups. In contrast, the US + N/P/M group exhibited a significantly larger area of Safranin-O and collagen II positivity, and deeper Toluidine Blue staining compared to the other three groups (Fig. 7D and E; Fig. S25, Supporting Information). At 8 weeks postoperatively, there was a further increase in fibrocartilage regeneration across all groups compared to the 4-week postoperative assessment, with the US + N/P/M group continuing to demonstrate the most pronounced fibrocartilage regeneration. Further semi-quantitative analysis for Safranin O-fast green staining and collagen II immunohistochemical staining also revealed consistent results (Fig. 7F; Fig. S26, Supporting Information). Collectively, these results indicated that N/P/M under US significantly improved tendon healing quality, tissue maturity, and collagen deposition postoperatively. Furthermore, these findings highlighted its promising therapeutic capacity in facilitating fibrocartilage quality and maturity in the tendon-to-bone healing process.

3.9. Ultrasound-induced piezoelectric stimulation facilitated vascular and bone regeneration and enhanced biomechanical strength

The restricted healing of the tendon-to-bone enthesis can be attributed to the diminished vascularization and the impaired bone integration, which are crucial steps in the ingrowth of bone into the tendon and the formation of a continuous tendon-to-bone interface [31]. Thus, we assessed the vascular regeneration at the tendon-to-bone interface using immunofluorescence staining for VEGF and α -SMA at 4 and 8 weeks postoperatively. As depicted in Fig. 8A, at 4 weeks postoperatively, the control, US, and N/P/M groups exhibited minimal positivity for α -SMA and VEGF staining, while the US + N/P/M group demonstrated a higher

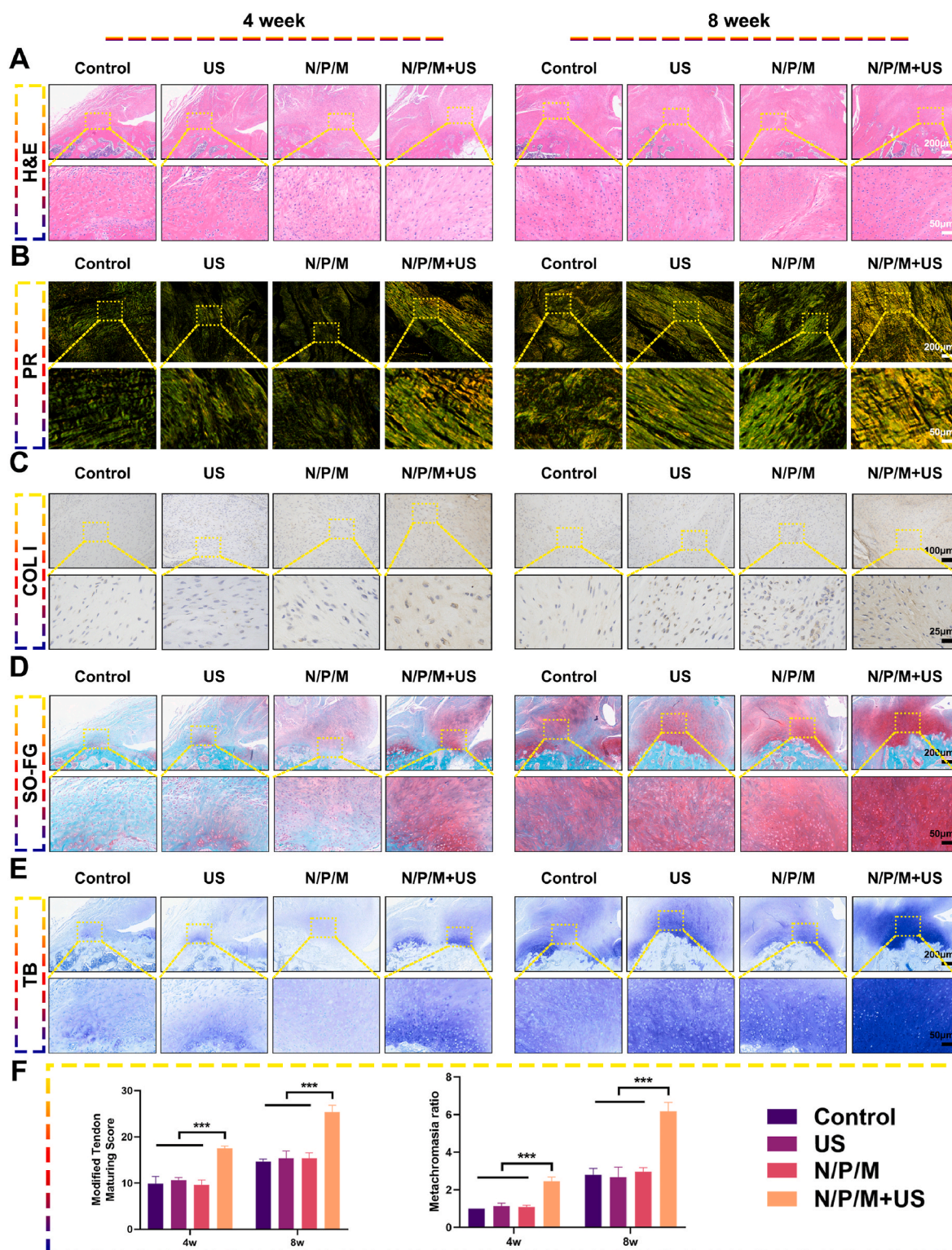


Fig. 7. Ultrasound-induced piezoelectric stimulation promoted the supraspinatus tendon repair and fibrocartilage layer reconstruction in a rat RCR model. A) H&E staining images at the tendon-to-bone interface at 4 weeks and 8 weeks postoperatively. B) Picrosirius red (PR) staining of the tendon-to-bone interface at 4 weeks and 8 weeks postoperatively. C) Immunohistochemical staining for Collagen I (COL I) at the tendon-to-bone interface at 4 weeks and 8 weeks postoperatively. D) Safranin O-fast green (SO-FG) staining of the tendon-to-bone interface at 4 weeks and 8 weeks postoperatively. E) Toluidine blue (TB) staining at the tendon-to-bone interface at 4 weeks and 8 weeks postoperatively. F) Histological score of supraspinatus tendon and semi-quantitative analysis of SO-FG staining at 4 weeks and 8 weeks postoperatively. n = 6. *p < 0.05, **p < 0.01, and ***p < 0.001.

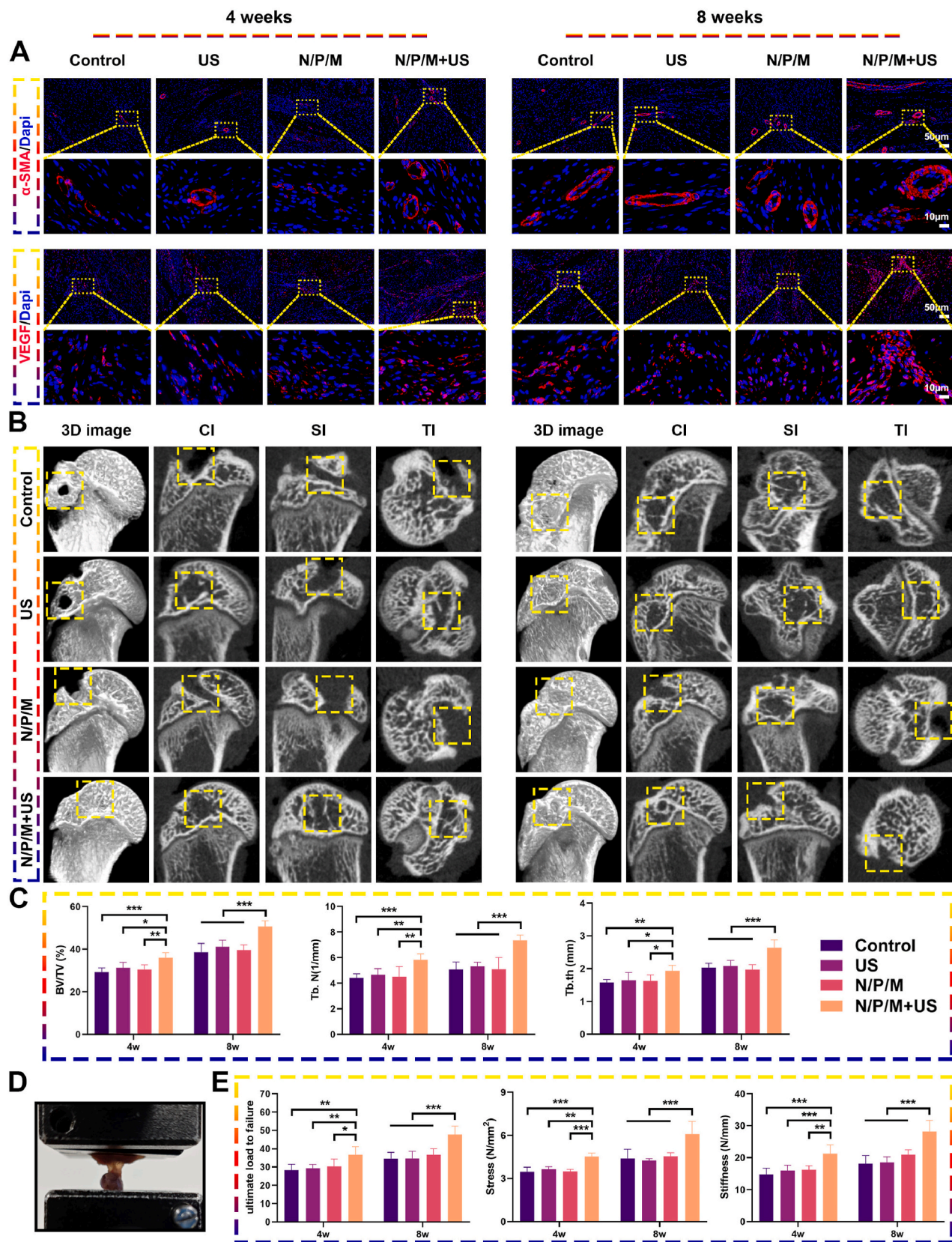


Fig. 8. Ultrasound-induced piezoelectric stimulation promoted vascular and new bone formation and increased the biomechanical properties of supraspinatus-humerus complex. A) Typical immunofluorescence images of α -SMA and VEGF at the tendon-to-bone interface at 4 weeks and 8 weeks postoperatively. B) Micro-CT analysis of the proximal humerus at 4 weeks and 8 weeks postoperatively. C) BV/TV, Tb. N, and Tb.th analysis at 4 weeks and 8 weeks postoperatively. D) Images of biomechanical testing for the supraspinatus-humerus complex postoperatively. E) Ultimate load, stress, and stiffness analysis for the supraspinatus-humerus complex at 4 weeks and 8 weeks postoperatively. n = 6. *p < 0.05, **p < 0.01, and ***p < 0.001.

number of α -SMA positive vessels and VEGF expression. By 8 weeks postoperatively, there was a further increase in α -SMA and VEGF expression across all groups, with the US + N/P/M group showing the most obvious α -SMA and VEGF protein expression. Semi-quantitative analysis of the fluorescence intensity for α -SMA and VEGF further substantiates the significant angiogenic capacity of US + N/P/M group (Fig. S27, Supporting Information). Additionally, the US + N/P/M group demonstrated significantly larger microvascular diameters, indicating enhanced vascular maturity and increased vascular density. These findings were also consistent with the upregulation of VEGF signaling pathway observed in proteomic analysis, likely attributable to the early inflammatory modulatory effects of N/P/M under US, thereby promoting the regeneration of mature and functional vessels and ultimately aiding in tendon-to-bone interface healing.

Subsequently, we employed micro-computed tomography (micro-CT) to analyze new bone formation in the bone tunnels of each group postoperatively (Fig. 8B). At both 4 and 8 weeks postoperatively, the US + N/P/M group demonstrated a significantly reduced bone tunnel size compared to the other three groups. There was no statistical difference in the bone tunnel size between the control group, US group and N/P/M group at the two observation time points. Further analysis of BV/TV and Tb. N for all four groups was conducted (Fig. 8C). No significant differences were observed between the control, US, and N/P/M groups at either time point; in contrast, the US + N/P/M group exhibited a significant increase in BV/TV and Tb. N. Specifically, at 8 weeks postoperatively, the BV/TV and Tb. N were as follows: control group ($38.59 \pm 3.72\%$, 5.08 ± 0.52 1/mm), US group ($41.14 \pm 2.84\%$, 5.32 ± 0.29 1/mm), N/P/M group ($39.65 \pm 2.19\%$, 5.11 ± 0.82 1/mm), and US + N/P/M group ($50.64 \pm 2.53\%$, 7.36 ± 0.37 1/mm). Further analysis of Tb.th and Tb.sp revealed that the US + N/P/M group had highest Tb.th and lowest Tb.sp values compared to the other groups, with no significant differences observed among the remaining three groups (Fig. 8C; Fig. S28, Supporting Information). Collectively, these results indicated that the US + N/P/M group significantly promoted neovascularization and new bone formation at the tendon-to-bone interface, potentially overcoming the challenges of poor vascularization and limited bone integration during tendon-to-bone healing.

The primary function of the tendon-to-bone enthesis is to facilitate the efficient transmission of mechanical stress from the tendon to the bone [40]. Therefore, a well-healed tendon-to-bone interface should promote the improvement of the mechanical function, which is essential in decreasing the retear rate. Biomechanical testing was performed to assess the mechanical properties of the supraspinatus tendon-humeral complex at 4 and 8 weeks postoperatively (Fig. 8D). Firstly, no statistical differences were observed in the cross-sectional area of the supraspinatus tendon among all groups at both time points (Fig. S29, Supporting Information). The failure load (N) of the complexes showed a time-dependent increase from week 4 to week 8 in all groups postoperatively (Fig. 8E). Moreover, there were no significant differences in failure load between the control group (28.22 ± 2.93 at 4 weeks, 34.64 ± 3.06 at 8 weeks), the US group (29.28 ± 1.90 at 4 weeks, 33.06 ± 3.84 at 8 weeks), and the N/P/M group (30.24 ± 3.76 at 4 weeks, 36.66 ± 3.06 at 8 weeks). In contrast, the US + N/P/M group (36.75 ± 3.90 at 4 weeks, 47.76 ± 4.12 at 8 weeks) demonstrated significantly higher failure loads at both time points. This finding might be attributed to the beneficial effects of N/P/M under US in increasing new bone formation and enhancing the structural integrity of the tendon-to-bone interface. Additionally, considering that there were no significant differences in tendon cross-sectional area among the groups, the differences in failure load were primarily due to the quality of the tendon-to-bone interface rather than the tendon size. Further analysis of the stress and stiffness values of the complexes revealed that the stress (N/mm²) and stiffness (N/mm) values also increased with the extension of healing time in all groups (Fig. 8E). Specifically, the US + N/P/M group indicated the highest stress values at both time points (4.53 ± 0.23 at 4 weeks, 6.10 ± 0.80 at 8 weeks) among all groups. The control group (3.46 ± 0.30 at 4

weeks, 4.37 ± 0.21 at 8 weeks), the US group (3.65 ± 0.15 at 4 weeks, 4.25 ± 0.12 at 8 weeks), and the N/P/M group (3.49 ± 0.13 at 4 weeks, 4.53 ± 0.24 at 8 weeks) did not show statistical differences in the stress values. The results suggested that the effects of N/P/M under US not only improved mechanical strength but also contributed to stress dissipation, which both played vital roles in reducing the postoperative retear. Furthermore, the US + N/P/M group also demonstrated the highest stiffness values at both time points (21.29 ± 2.51 at 4 weeks, 28.19 ± 3.19 at 8 weeks). The control group (14.72 ± 1.86 at 4 weeks, 18.12 ± 2.31 at 8 weeks), the US group (15.96 ± 1.51 at 4 weeks, 18.52 ± 1.57 at 8 weeks), and the N/P/M group (16.18 ± 1.54 at 4 weeks, 20.99 ± 1.36 at 8 weeks) exhibited no significant differences in stiffness values. These biomechanical data robustly indicated that N/P/M under US markedly enhanced the biomechanical performance of the enthesis, potentially improving the therapeutic outcomes after RCR. At week 8 postoperatively, H&E staining from major organs in all groups revealed no significant adverse effects, demonstrating the superior *in vivo* biosafety profile of N/P/M (Fig. S30, Supporting Information).

We demonstrated that N/P/M under US can promote tendon-to-bone healing by achieving early inflammation modulation and angiogenesis, as evidenced by the rat RCR model. It is noteworthy that tendon-to-bone healing is a complex process also involving various functional cells, such as mesenchymal stem cells (MSCs). Additionally, previous studies were reported that piezoelectric stimulation might enhance the differentiation and function of stem cells, which were also essential for tendon-to-bone repair [13a,13b]. Future work will further elucidate the potential effects of N/P/M under US on stem cells related to the enthesis healing and explore the underlying mechanisms, thereby optimizing the efficacy of N/P/M under US for RCR and its potential applications in tissue regeneration.

4. Conclusion

In summary, we developed a novel Janus asymmetric piezoelectric adhesive that can be readily applied in RCR through a simple adhesion procedure and exhibited outstanding electrical stimulation effects under ultrasound stimulation. The piezoelectric adhesives were demonstrated to have superior anti-inflammatory effects on THP-1 cells and human rotator cuff tear samples, attributed to the activation of macrophage TRPV1 channels, subsequently triggering cAMP signaling pathway and effectively inhibiting macrophages polarization towards M1 phenotype, as evidenced by RNA sequencing. Furthermore, the piezoelectric adhesives were shown to alleviate the suppressive effects of the inflammatory environment on HUVECs angiogenesis. Early postoperative proteomic analysis revealed the downregulation of inflammatory signaling pathways (ArA metabolism and TNF- α signaling pathway) and the upregulation of VEGF signaling pathway, further elucidating the potential mechanisms by which the piezoelectric adhesives promoted tendon-to-bone healing *in vivo*. The application of the piezoelectric adhesives eventually enhanced the histological repair of the enthesis and strengthened biomechanical strength, offering a simple, feasible, and promising tissue engineering platform for the clinical treatment of rotator cuff healing, with significant therapeutic potential.

CRedit authorship contribution statement

Moran Huang: Writing – original draft, Investigation, Data curation, Conceptualization. **Wan Li:** Writing – original draft, Methodology, Data curation, Conceptualization. **Yaying Sun:** Writing – review & editing, Methodology, Investigation. **Jize Dong:** Investigation, Formal analysis. **Chaojing Li:** Supervision, Methodology, Investigation. **Henjie Jia:** Software. **Yongjie Jiao:** Resources, Investigation. **Lu Wang:** Supervision, Resources. **Shanxing Zhang:** Writing – review & editing, Supervision, Project administration. **Fujun Wang:** Writing – review & editing, Supervision, Funding acquisition. **Jiwu Chen:** Writing – review & editing, Project administration, Funding acquisition, Conceptualization.

Ethics approval and consent to participate

The collection of supraspinatus tendon samples was approved by the Ethics Committee of Shanghai General Hospital, and informed consent was obtained from all participants (2022KY014C23-1).

The animal study was approved by the Institutional Animal Care and Use Committee of Shanghai General Hospital (AD2024090).

Declaration of competing interest

The authors declare that they have no known competing financial interests or personal relationships that could have appeared to influence the work reported in this paper.

Acknowledgement

This work was financially supported by the National Natural Science Foundation of China (Grant No. 82372491, 82172509, 82102634, and 32371402).

Appendix A. Supplementary data

Supplementary data to this article can be found online at <https://doi.org/10.1016/j.bioactmat.2025.03.029>.

References

- [1] A. Bedi, J. Bishop, J. Keener, D.A. Lansdown, O. Levy, P. MacDonald, N. Maffulli, J. H. Oh, V.J. Sabesan, J. Sanchez-Sotelo, R.J. Williams 3rd, B.T. Feeley, *Nat. Rev. Dis. Primers* 10 (2024) 8.
- [2] M. Amini, E. Ricchetti, J. Iannotti, K. Derwin, *Orthop. Res. Rev.* 7 (2015) 57.
- [3] K. Atesok, F.H. Fu, M.R. Wolf, M. Ochi, L.M. Jazrawi, M.N. Doral, J.H. Lubowitz, S. A. Rodeo, *J. Bone Joint Surg. Am.* 96 (2014) 513.
- [4] a) E. Pugliese, A. Rossoni, D.I. Zeugolis, *Biomater. Adv.* 157 (2024) 213740; b) F. Fang, A.G. Schwartz, E.R. Moore, M.E. Sup, S. Thomopoulos, *Sci. Adv.* 6 (2020).
- [5] a) H. Gao, L. Wang, Z. Lin, H. Jin, Y. Lyu, Y. Kang, T. Zhu, J. Zhao, J. Jiang, *Materials today. Bio* 22 (2023) 100749; b) X. Tong, T. Zhang, S. Li, Y. Chen, Y. Xu, C. Deng, J. Hu, H. Lu, *J. Orthopaedic Trans.* 38 (2023) 65.
- [6] S. Liu, L. Zhang, Z. Li, F. Gao, Q. Zhang, A. Bianco, H. Liu, S. Ge, B. Ma, 2024, 34, 2306534.
- [7] a) Y. Liu, Q. Guo, X. Zhang, Y. Wang, X. Mo, T. Wu, *Adv. Fiber Mater.* 5 (2023) 1241; b) W. Liu, H. Zhao, C. Zhang, S. Xu, F. Zhang, L. Wei, F. Zhu, Y. Chen, Y. Chen, Y. Huang, M. Xu, Y. He, B.C. Heng, J. Zhang, Y. Shen, X. Zhang, H. Huang, L. Chen, X. Deng, *Nat. Commun.* 14 (2023) 4091.
- [8] W.A. Catterall, G. Wisedchaisri, N. Zheng, *Nat. Chem. Biol.* 13 (2017) 455.
- [9] a) C.T. Brighton, W. Wang, C.C. Clark, *J. Bone Joint Surg. Am.* 90 (2008) 833; b) G. Victoria, B. Petrisor, B. Drew, D. Dick, *Indian J. Orthop.* 43 (2009) 117.
- [10] a) M. Liu, W. Zhang, S. Han, D. Zhang, X. Zhou, X. Guo, H. Chen, H. Wang, L. Jin, S. Feng, Z. Wei, 2024, 36, 2313672; b) X. Liu, X. Wan, B. Sui, Q. Hu, Z. Liu, T. Ding, J. Zhao, Y. Chen, Z.L. Wang, L. Li, *Bioact. Mater.* 35 (2024) 346.
- [11] a) L. Chen, C. Yu, W. Xu, Y. Xiong, P. Cheng, Z. Lin, Z. Zhang, L. Knoedler, A. C. Panayi, S. Knoedler, J. Wang, B. Mi, G. Liu, *ACS Nano* 17 (2023) 3153; b) W. Song, Y. Guo, W. Liu, Y. Yao, X. Zhang, Z. Cai, C. Yuan, X. Wang, Y. Wang, X. Jiang, H. Wang, W. Yu, H. Li, Y. Zhu, L. Kong, Y. He, *Adv. Mater.* 36 (2024) e2408255.
- [12] a) H.G. Yi, K.S. Kang, J.M. Hong, J. Jang, M.N. Park, Y.H. Jeong, D.W. Cho, *J. Biomed. Mater. Res.* 104 (2016) 1797; b) B. Ferrigno, R. Bordett, N. Duraisamy, J. Moskow, M.R. Arul, S. Rudraiah, S. P. Nukavarapu, A.T. Vella, S.G. Kumar, *Bioact. Mater.* 5 (2020) 468.
- [13] a) Y. Liu, G. Dzidotor, T.T. Le, T. Vinikoor, K. Morgan, E.J. Curry, R. Das, A. McClinton, E. Eisenberg, L.N. Apuzzo, K.T.M. Tran, P. Prasad, T.J. Flanagan, S. W. Lee, H.M. Kan, M.T. Chorsi, K.W.H. Lo, C.T. Laurencin, T.D. Nguyen, *Sci. Transl. Med.* 14 (2022) eabi7282; b) T. Vinikoor, G.K. Dzidotor, T.T. Le, Y. Liu, H.M. Kan, S. Barui, M.T. Chorsi, E. J. Curry, E. Reinhardt, H. Wang, P. Singh, M.A. Merriman, E. D'Orio, J. Park, S. Xiao, J.H. Chapman, F. Lin, C.S. Truong, S. Prasad, L. Chuba, S. Killoh, S. W. Lee, Q. Wu, R.M. Chidambaram, K.W.H. Lo, C.T. Laurencin, T.D. Nguyen, *Nat. Commun.* 14 (2023) 6257; c) D. Liu, X. Wang, C. Gao, Z. Zhang, Q. Wang, Y. Pei, H. Wang, Y. Tang, K. Li, Y. Yu, Q. Cai, X. Zhang, *Adv. Mater.* 36 (2024) e2409400.
- [14] a) E.S. Hosseini, S. Dervin, P. Ganguly, R. Dahiya, *ACS Appl. Bio Mater.* 4 (2021) 163; b) S. Guerin, S.A.M. Tofail, D. Thompson, *NPG Asia Mater.* 11 (2019) 10; c) T.J. Haley, N. Komesu, K. Raymond, *Toxicol. Appl. Pharmacol.* 4 (1962) 385.
- [15] R. Das, T.T. Le, B. Schiff, M.T. Chorsi, J. Park, P. Lam, A. Kemerley, A.M. Supran, A. Eshed, N. Luu, N.G. Menon, T.A. Schmidt, H. Wang, Q. Wu, M. Thirunavukkarasu, N. Maulik, T.D. Nguyen, *Biomaterials* 301 (2023) 122270.
- [16] S. Tang, K. Feng, R. Yang, Y. Cheng, M. Chen, H. Zhang, N. Shi, Z. Wei, H. Ren, Y. Ma, *Adv. Healthcare Mater.* (2024) e2403734.
- [17] S. Choi, J.R. Moon, N. Park, J. Im, Y.E. Kim, J.H. Kim, *Adv. Mater.* 35 (2023) e2206207.
- [18] F.X. Zhang, P. Liu, W. Ding, Q.B. Meng, D.H. Su, Q.C. Zhang, R.X. Lian, B.Q. Yu, M. D. Zhao, J. Dong, Y.L. Li, L.B. Jiang, *Biomaterials* 278 (2021) 121169.
- [19] B.R. Freedman, A. Kuttler, N. Beckmann, S. Nam, D. Kent, M. Schuleit, F. Ramazani, N. Accart, A. Rock, J. Li, M. Kurz, A. Fisch, T. Ullrich, M.W. Hast, Y. Tinguely, E. Weber, D.J. Mooney, *Nat. Biomed. Eng.* 6 (2022) 1167.
- [20] a) Z. Zheng, X. Chen, Y. Wang, P. Wen, Q. Duan, P. Zhang, L. Shan, Z. Ni, Y. Feng, Y. Xue, X. Li, L. Zhang, J. Liu, *Adv. Mater.* 36 (2024) e2408538; b) S. Pal, J. Shin, K. DeFrates, M. Arslan, K. Dale, H. Chen, D. Ramirez, P. B. Messersmith, *Science* 385 (2024) 877.
- [21] Z. Cai, C. Qu, W. Song, H. Wang, S. Chen, C. Zhou, C. Fan, *Adv. Mater.* 36 (2024) e2404842.
- [22] a) J. Zhao, T. Li, H. Sun, Z. Lu, T. Xiong, D. Li, D. Sun, *Adv. Compos. Hybrid Mater.* 7 (2024) 218.b) D. Xu, S. Fu, H. Zhang, W. Lu, J. Xie, J. Li, H. Wang, Y. Zhao, R. Chai, 2024, 36, 2307896. c) Y. Jiao, C. Li, S. Li, X. Liu, S. Yu, X. Liu, Y. Li, F. Wang, J. Tang, L. Wang, 2023, 33, 2305714.
- [23] Z. Xin, G. Lin, H. Lei, T.F. Lue, Y. Guo, *Transl. Androl. Urol.* 5 (2016) 255.
- [24] W.L. Lim, L.L. Liao, M.H. Ng, S.R. Chowdhury, J.X. Law, *Tissue Eng. Regen. Med.* 16 (2019) 549.
- [25] a) C. Cai, X. Zhang, Y. Li, X. Liu, S. Wang, M. Lu, X. Yan, L. Deng, S. Liu, F. Wang, C. Fan, *Adv. Mater.* 34 (2022) e2106564; b) S. Wang, Y. Xiao, J. Tian, B. Dai, Z. Tao, J. Liu, Z. Sun, X. Liu, Y. Li, G. Zhao, Y. Cui, F. Wang, S. Liu, *Adv. Mater.* 36 (2024) e2311964.
- [26] a) B. Zhang, H. Chen, J. Ouyang, Y. Xie, L. Chen, Q. Tan, X. Du, N. Su, Z. Ni, L. Chen, *Autophagy* 16 (2020) 1262; b) H. Qin, Z. Luo, Y. Sun, Z. He, B. Qi, Y. Chen, J. Wang, C. Li, W. Lin, Z. Han, Y. Zhu, *Int. J. Biol. Sci.* 19 (2023) 1123.
- [27] A.P. Koivisto, M.G. Belvisi, R. Gaudet, A. Szallasi, *Nat. Rev. Drug Discov.* 21 (2022) 41.
- [28] a) Q. Yan, C. Gao, M. Li, R. Lan, S. Wei, R. Fan, W. Cheng, *Int. J. Mol. Sci.* 25 (2024); b) Y. Yin, P. Zhao, X. Xu, B. Zhou, J. Chen, X. Jiang, Y. Liu, Y. Wu, W. Yue, H. Xu, W. Bu, *Adv. Mater.* 36 (2024) e2403979.
- [29] Z. Lv, X. Xu, Z. Sun, Y.X. Yang, H. Guo, J. Li, K. Sun, R. Wu, J. Xu, Q. Jiang, S. Ikegawa, D. Shi, *Cell Death Dis.* 12 (2021) 504.
- [30] a) Y. Shi, W. Tao, W. Yang, L. Wang, Z. Qiu, X. Qu, J. Dang, J. He, H. Fan, *J. Nanobiotechnol.* 22 (2024) 47; b) L.P. Tavares, G.L. Negreiros-Lima, K.M. Lima, E.S. Pmr, V. Pinho, M. M. Teixeira, L.P. Sousa, *Pharmacol. Res.* 159 (2020) 105030.
- [31] J. Zou, W. Wang, W. Cui, C. Li, C. Ma, X. Ji, J. Hong, Z. Qu, J. Chen, A. Liu, H. Wu, *J. Nanobiotechnol.* 21 (2023) 14.
- [32] W. Chen, Y. Sun, X. Gu, J. Cai, X. Liu, X. Zhang, J. Chen, Y. Hao, S. Chen, *Biomaterials* 271 (2021) 120714.
- [33] Y. Zhang, R. Sheng, J. Chen, H. Wang, Y. Zhu, Z. Cao, X. Zhao, Z. Wang, C. Liu, Z. Chen, P. Zhang, B. Kuang, H. Zheng, C. Shen, Q. Yao, W. Zhang, *Adv. Mater.* 35 (2023) e2210517.
- [34] P.A. Guerette, S. Hoon, Y. Seow, M. Raida, A. Masic, F.T. Wong, V.H. Ho, K. W. Kong, M.C. Demirel, A. Pena-Francesch, S. Amini, G.Z. Tay, D. Ding, A. Miserez, *Nat. Biotechnol.* 31 (2013) 908.
- [35] B. Su, J.P. O'Connor, *J. Appl. Physiol.* 115 (2013) 892 (Bethesda, Md. : 1985).
- [36] a) J. Chen, T. Yin, X. Hu, L. Chang, Y. Sang, L. Xu, W. Zhao, L. Liu, C. Xu, Y. Lin, Y. Li, Q. Wu, D. Li, Y. Li, M. Du, *Cell Rep.* 43 (2024) 114881; b) X. Liu, Q. Tao, Y. Shen, X. Liu, Y. Yang, N. Ma, J. Li, *Front. Pharmacol.* 14 (2023) 1220780.
- [37] A. Stahl, D. Hao, J. Barrera, D. Henn, S. Lin, S. Moeinzadeh, S. Kim, W. Maloney, G. Gurtner, A. Wang, Y.P. Yang, *Bioact. Mater.* 19 (2023) 167.
- [38] Z. Huang, Y. Zhang, R. Liu, Y. Li, M. Rafique, A.C. Midgley, Y. Wan, H. Yan, J. Si, T. Wang, C. Chen, P. Wang, M. Shafiq, J. Li, L. Zhao, D. Kong, K. Wang, *Biomaterials* 291 (2022) 121901.
- [39] a) P.T. Jensen, K.L. Lamberts, L.H. Frich, *J. Shoulder Elbow Surg.* 27 (2018) 739; b) S. Thomopoulos, G.M. Genin, L.M. Galatz, *J. Musculoskelet. Neuronal Interact.* 10 (2010) 35.
- [40] G.M. Genin, S. Thomopoulos, *Nat. Mater.* 16 (2017) 607.